A thesis presented for the degree of
Master of Science

The gas content of Luminous Compact Blue Galaxies in the COSMOS field

Author:
Henco Arlow

Supervisors:
Prof. D.J. Pisano
Prof. Matthew Bershady

Department of Astronomy
University of Cape Town

May 2, 2024

Abstract

Luminous compact blue galaxies (LCBGs) are a heterogeneous subset of starburst galaxies. Their number density drops quite significantly as we approach lower redshifts. As a set of galaxies that evolve quickly, they make excellent candidates for studying galactic evolution as a whole. In order to understand how galaxies evolve, we make use of LCBGs to study their gas content as it changes over approximately nine billion years of lookback time. We make use of HI emission line data provided by the full CHILES survey, covering a redshift range of z=0 to z=0.45 within the COSMOS field as well as continuum data of the same field provided by the CHILES Continuum Polarization survey.

In this thesis we set out to study the properties of LCBGs in these fields to better understand the nature of these objects as they evolve to the present day. We report on direct detections of HI found in LCBGs in CHILES. We also perform a cubelet stacking technique on LCBGs for which we have known spectroscopic redshifts in CHILES. From these stacks we measure average HI masses as well as upper limit values for non-detections to study how it evolves with redshift. We also measure the star formation rates of a set of LCBGs using continuum fluxes in CHILES Con Pol and compare our results to measurements made with data from CHILES's first epoch. Continuum stacking is then performed in several redshift and stellar mass bins to extract average star formation rates. We proceed to fit appropriate functions to these relations in order to quantify the dependence of LCBG sSFRs to their stellar mass and redshift.

Acknowledgements

I would firstly like to thank Prof. D.J. Pisano and Prof. Matthew Bershady for their guidance, support and the opportunities I was given as I freshly entered the world of radio astronomy. I would like to express gratitude to Dr. Nicholas Luber for developing and supplying me with his stacking code which I could use and adapt for this thesis and to Dr. Lucas Hunt for his catalog of LCBGs. They also provided me with very valuable advice throughout the project.

A big word of thanks to my friends and colleagues in the UCT Department of Astronomy and at SAAO for advice, support and general words of encouragement. Finally, thank you to my family for the continuous love and for standing behind me as I pursue my dream of becoming an astrophysicist.

This work made use of the CARTA (Cube Analysis and Rendering Tool for Astronomy) software (DOI 10.5281/zenodo.3377984 – https://cartavis.github.io).

This work was supported by the South African Research Chairs Initiative and the South African National Research Foundation. The financial assistance of the South African Radio Astronomy Observatory (SARAO) towards this research is hereby acknowledged (www.sarao.ac.za).

Contents

List of Figures

List of Tables

Chapter 1

Introduction

1.1 The evolution of galaxies

When we observe the sky beyond the Milky Way, one of the most striking features of our universe is the enormous diversity of galaxies out there. Over billions of years since the Big Bang, the same uniformly distributed matter managed to arrange itself into a breathtaking collection of different morphologies and structures. As scientists started observing them, it quickly became apparent that these objects require rigorous classification if we wanted to understand them. An early example of such a classification scheme is the Hubble sequence (shown in Figure 1) proposed by Hubble in 1926. This scheme grouped galaxies according to key physical attributes when observed in the optical. Traditionally it starts by depicting elliptical galaxies on the left. These are radially symmetric galaxies that show no apparent structure beyond being elliptical in shape. These galaxies vary in ellipticity given by $e = 1 - \frac{a}{b}$, where a and b are its semi-major and semi-minor axes. Next we find lenticular galaxies. These are similar to ellipticals, but they contain a central bar or bulge where stars are more densely packed. The most striking of the classes are spiral galaxies, which are disk-shaped galaxies containing denser regions in the form of a spiral. These spirals can vary in structure and often contain prominent central bars as well, in which case they are classified as barred spirals. Finally we have irregular galaxies which fit none of the above mentioned classifications. These galaxies have no discernible structure.

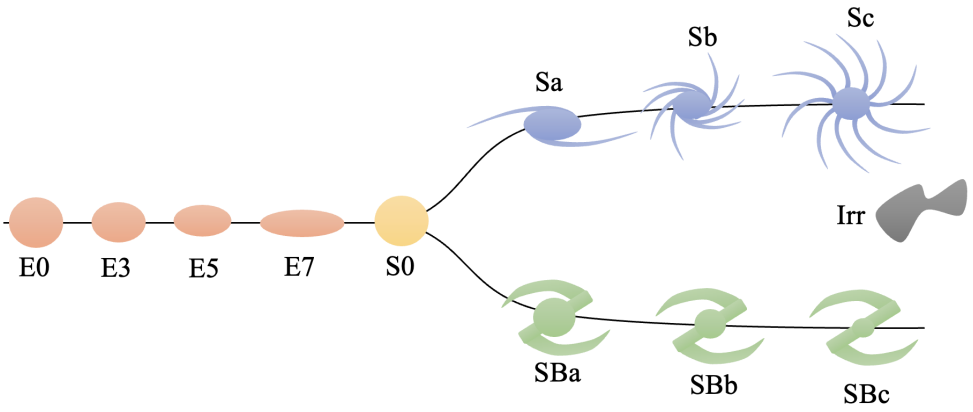

Figure 1: A diagram of the Hubble sequence, which is used to classify galaxies till this day. Ellipticals are denoted with and 'E' along with a number representing its ellipticity. Lenticulars are represented by 'S0'. Spirals are represented by 'Sa', 'Sb' or 'Sc', depending on the tightness of the spirals. Barred spirals are represented by 'SBa', 'SBb' or 'SBc', depending on the brightness of its bulge. Irregulars are represented by 'Irr'.

Let us first take a step back and ask ourselves how galaxies began to form in the first place. It is believed that it all started from the very first quantum fluctuations in the primordial universe. These fluctuations gave rise to the evolution and growth of perturbations in the early universe (Cimatti et al. 2019). We are assuming that the the perturbations were happening in a universe mainly consisting out of non-relativistic dark matter. Denser regions attracted each other and less dense regions became more under-dense. As these perturbations grew due to these gravitational instabilities, larger structures of dark matter formed that eventually became virialised. We refer to these structures as 'dark matter halos' (Schneider 2006). Diffuse, neutral, pre-galactic gas collapsed within these halos. This gas had to be cooled efficiently enough to eventually form what we call Population III stars. These formed at $z \approx 20 - 30$ in lower mass 'mini-halos' (Cimatti et al. 2019). These stars would then enrich the intergalactic medium (IGM) through supernova explosions. Higher mass halos accreted the gas expelled from Population III stars and formed their own stars within them. This constitutes the first galaxies at $z \approx 10$ (Cimatti et al. 2019). Again, the cooling of the infalling gas has to be efficient, since condensation will be delayed by the pressure of hot gas. The main contributor to this cooling is radiation, triggered by collisions and scattering of

atoms and electrons. There is an interplay between the cooling time of the gas, in which it would loose all its energy, and the free-fall time i.e., the time for a gas particle to reach the center of the collapsing cloud. Efficient cooling occurs when the cooling time is less than the free-fall time. The cooling efficiency and the mass of the dark matter halo determine whether a galaxy would ultimately be formed.

Looking at the rich set of galaxies we observe today, it was evident that these first galaxies were likely evolving from one form to another, but how this process was playing out was the key question. While spirals and irregulars still dominate today, the number of ellipticals have increased significantly and are much more common than in the early universe. What this suggests, is that galaxies initially formed into spirals and irregulars and then, through some mechanism, gradually evolved into ellipticals. To add to this theory, irregular and spiral galaxies contain blue, young stars, whereas ellipticals are populated by much older, redder stars. The leading consensus to what causes this transition in morphology are interactions and mergers between galaxies (Mo et al. 2010). Galaxies range from being isolated to belonging to clusters. This means galaxies can interact gravitationally, disturbing each others morphologies, or even merge to form one galaxy. We observe more elliptical galaxies in the denser regions of clusters where interactions are more likely. Over 50% of disk galaxies are warped which are likely from past galaxy interactions (Carroll & Ostlie 2017). Some ellipticals also show shell-like structures, which are believed to be the result of mergers. Interactions are thus a major driver of evolution. There are a range of ways there interactions can take place. Astronomers firstly make a distinction between mergers which depend on the mass ratio of the merging galaxies. If one galaxy is much larger than the other we speak of a 'minor' merger, otherwise if they are roughly the same in mass, we call it a 'major' merger. The interaction of merging galaxies are also heavily dependent on the gas mass fraction of each. If both are gas-rich or gas-poor the interaction is referred to as a 'wet' or a 'dry' merger respectively (Mo et al. 2010).

To fully understand galaxy evolution, we must look at the constituents of a galaxy themselves and how they evolve. Most properties of a galaxy

are determined by the stars within them, but this is driven by the amount of cold neutral hydrogen gas (HI) available to form molecular hydrogen (H_2) which fuels stars. If we want to track the inner changes of a galaxy, we must track the HI gas. This is made possible through the observation of the HI spectral line (discussed in §1.2), HI stacking (discussed in §3.1.2), as well as the absorption of Lyman-α emission from distant quasi-stellar objects, QSOs, by HI in the intergalactic medium. Indicators of how HI in galaxies evolve is the HI mass function (HIMF) at a given epoch i.e., the number of galaxies within an HI mass bin per unit cosmic volume, and the cosmic HI density as a function of redshift. The measurement of the HIMF is still an ongoing endeavour of current surveys. The cosmic HI density, Ω_{HI} is the amount of HI per co-moving volume, normalised by the critical density of the universe (Chen et al. 2021*b*):

$$\Omega_{HI} = \frac{\rho_{HI}}{\rho_{crit}} \tag{1.1}$$

This quantity has been studied intensively across many redshifts using the aforementioned techniques. Through a myriad of estimations and simulations, it has been determined that the Ω_{HI} parameter evolves with redshift by $\Omega_{HI}(z) = 10^{-3.53}(1+z)^{0.74}$, as shown in section 5.5 of Davé et al. (2017). We show this evolution in Figure 2. We see little evolution at low redshifts between $0 < z < 1.5$ but then an increases by a factor of 3-4 when we look at high redshifts. We do not have much statistics on what happens at intermediate redshifts, because of current constraints with observing the HI spectral line directly. As for the mass function, Jones et al. (2018) measured the HIMS through the ALFALFA survey. The HIMF is best fit by a Schechter function:

$$\Phi(M_{HI}) = \ln(10)\Phi^* \left(\frac{M_{HI}}{M_*}\right)^{\alpha+1} \exp\left(-\frac{M_{HI}}{M_*}\right) \tag{1.2}$$

with Φ^* being the normalisation density, M_* is the characteristic mass between a power law component, of which α is the slope, and an exponential component. Jones et al. (2018) measured the following best fit parameters: $\Phi^* = (5.4 \pm 0.2) \times 10^{-3}$ Mpc^{-3}, $\alpha = -1.25 \pm 0.02$ and $\log(M_*/M_\odot) = 9.94 \pm 0.01$. We can compare this to the mass function at a higher redshift measurements at $z \approx 0.35$ done by Bera et al. (2022). From

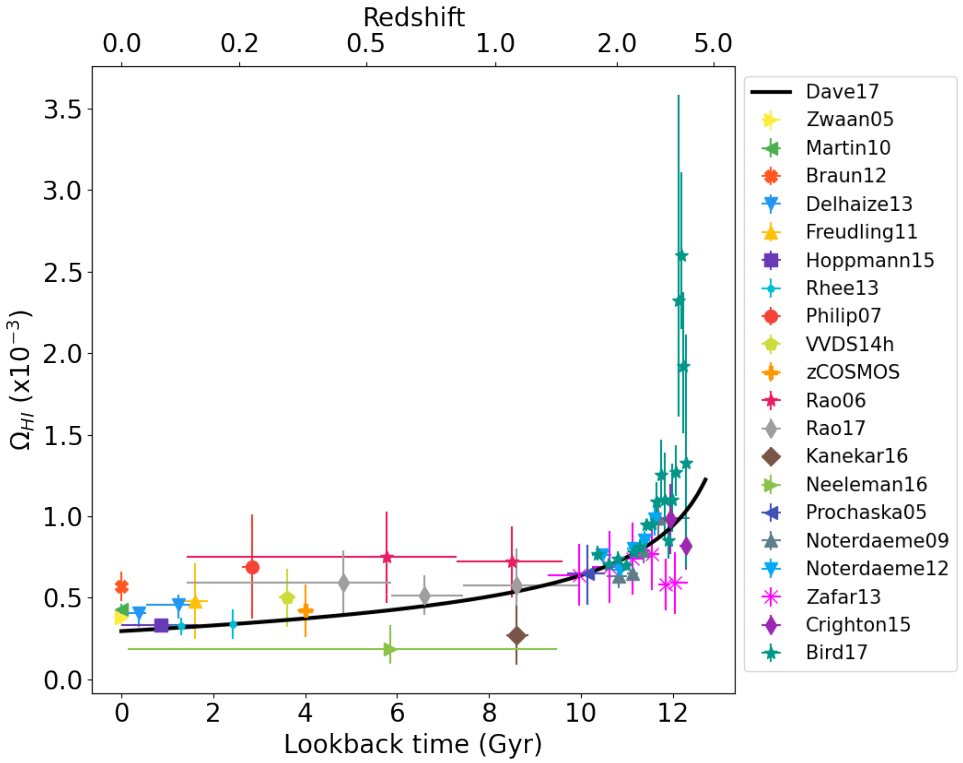

Figure 2: The evolution of cosmic neutral hydrogen density as a function of lookback time and redshift. The black line is from the Davé et al. (2017) model.

their sample, they measured $\Phi^* = (4.0 \pm 0.4) \times 10^{-3}$ Mpc^{-3}, $\alpha = 1.29 \pm 0.03$ and $\log(M_*/M_\odot) = 9.94 \pm 0.031$. They find a larger density of lower HI masses and a lower density of high HI masses at $z \approx 0.35$ when compared to $z \approx 0$. This could be an indication of merging events providing a substantial amount of HI to higher mass local galaxies.

Astronomers have run similar experiments to trace the star formation rates (SFR) of galaxies over cosmic time. SFRs can be estimated from a galaxy's luminosity at a range of wavelengths: Hα, UV, infrared and radio. By calculating the luminosity function at a given epoch, $\Phi(L, z)$, we can continue to determine the cosmic star formation rate density, ψ_{SFR} at said epoch (Cimatti et al. 2019):

$$\psi_{SFR} = C \int_0^\infty L\Phi(L, z)dL \tag{1.3}$$

where C is a coefficient determined by the wavelength of light which used to measure the SFR density. The best fit function to the evolution of ψ_{SFR}

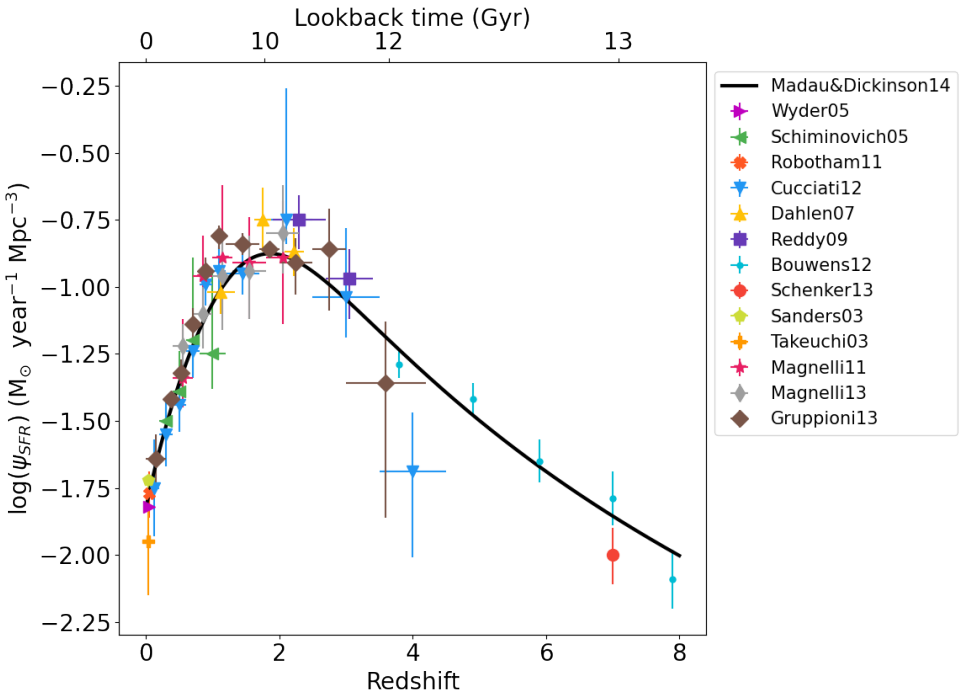

Figure 3: The evolution of cosmic star formation rate density over cosmic time. The solid black line is the best fit to the evolution by Madau & Dickinson (2014).

with redshift, see Figure 3, has been calculated to be

$$\psi_{SFR}(z) = 0.015\frac{(1+z)^{2.7}}{1+[(1+z)/2.9]^{5.6}}\ \mathrm{M}_\odot\ \mathrm{year}^{-1}\ \mathrm{Mpc}^{-3} \tag{1.4}$$

by Madau & Dickinson (2014).

We observe a steady increase in the density up until $z \approx 2$ where it reaches a maximum and then decreases again. This maximum is commonly referred to as 'cosmic noon'. From this we gather that the peak of star formation in the universe occurred at this time. Majority of stars follow a tight relation in terms of SFR and stellar mass. This is known as the star formation main sequence. There do however exist galaxies that lie off of this main sequence with SFRs higher than that of normal star forming galaxies. These are known as starburst galaxies. The origin of starbursts are likely due to merger events between galaxies of comparable size. This sends shock-waves through the gas resulting in an increased rate of star formation throughout the system. Of a sample of star forming galaxies studied by Rodighiero et al. (2011) at $z \sim 2$, only 2% were starbursts and they contributed to only around 10% of the cosmic star formation density

at this redshift. The evolution of starbursts is thus of interest to be studied independently of other star forming galaxies.

1.2 Observing neutral hydrogen

The observation of neutral hydrogen is made possible by emission from the hyperfine transition within the ground state of the atom. This is ultimately an interaction between the single proton in hydrogen's nucleus and the single electron. The electromagnetic interaction between the spins of these particles result in a two energy levels. When their relative spins flip, the atom releases a photon that we can detect. The frequency of the light emitted is given by:

$$\nu = \frac{8}{3} g_1 \left(\frac{m_e}{m_p} \right) \alpha^2 R_H c \tag{1.5}$$

Here g_1 is the nuclear g-factor associated with the nuclear magnetic moment of the proton, which has a value of $g_1 \approx 5.59$ (Condon & Ransom 2016). α is the fine structure constant,

$$\alpha = \frac{e^2}{\hbar c} \approx \frac{1}{137} \tag{1.6}$$

and $R_H c$ is the Rydberg frequency for hydrogen,

$$R_H c = c \left(\frac{m_e e^4}{8 \epsilon_0^2 h^3 c} \right) \left(1 + \frac{m_e}{m_p} \right)^{-1} \approx 3.288 \times 10^{15} \text{ Hz} \tag{1.7}$$

This results in a photon being emitted at $\nu \approx 1420.40575$ MHz or $\lambda \approx 21$ cm. This falls under the radio zone of the electromagnetic spectrum. The energy of the emitted photon is $E \approx 5.87$ μeV. This energy is so low, that almost all hydrogen atoms are found in the upper level state. This spin-flip transition is a forbidden one and is very rare. It's emission coefficient is $A_{ul} \approx 2.88 \times 10^{-15}$ s (Gould 1994), making the likelihood of a transition one in 11 million years. Luckily, hydrogen is the most abundant element in the universe, making emission from HI detectable here on earth. Radio emission can penetrate dust in the Milky Way, making it possible to detect HI regardless of what is in the intermediate interstellar medium. The atmosphere of the Earth is also transparent in the radio spectrum, making

observations possible through the use of ground based telescopes. The physics of the HI line makes it possible to detect neutral hydrogen in nearby galaxies. What makes it remarkably useful at this scale, is that we can use the frequency at which we measure the line to calculate the radial velocity and the distance of the galaxy. Note that this is assuming the velocity due to the expansion of the universe is much larger than the radial velocity of the galaxy's peculiar motion. The radial velocity is related to the galaxies redshift:

$$v_r = cz = c\left(\frac{1420.40575}{\nu_o} - 1\right) \tag{1.8}$$

Here ν_o is the observed frequency of the hyperfine line. Our understanding of cosmology today, makes it possible to calculate the luminosity distance of the galaxy. For a given cosmology, the luminosity distance of a galaxy is given by,

$$D_L = (1+z)\int_0^z \frac{dz'}{H(z')} \tag{1.9}$$

The luminosity distance fundamentally determines the bolometric flux that we would observe from an object radiating at a certain luminosity. As we can see, we just require to specify the dynamics of our cosmology to choose a value for the Hubble parameter. Assuming a flat ΛCDM model, the Hubble parameter (Ryden 2017) is:

$$H(z) = H_0\sqrt{\Omega_r(1+z)^4 + \Omega_m(1+z)^3 + \Omega_\Lambda} \tag{1.10}$$

Now that we have a distance, we can calculate the mass of the HI in our line of sight. We calculate the integrated flux from HI mission and convert it to a luminosity density through this luminosity distance. The flux is only proportional to the hydrogen column density, and hence the mass, if the emission is optically thin. These quantities are calculated as follows:

$$\frac{M_{HI}}{M_\odot} = 49.8\left(\frac{D_L}{\text{Mpc}}\right)^2 \int \frac{S(\nu)}{\text{Jy}}\left(\frac{d\nu}{\text{Hz}}\right) \tag{1.11}$$

$$\frac{N_{HI}}{\text{cm}^{-2}} = \frac{2.34\times10^{20}}{\theta_1\theta_2}(1+z)^4 \int \frac{S(\nu)}{\text{Jy}}\left(\frac{d\nu}{\text{Hz}}\right) \tag{1.12}$$

where θ_1 and θ_2 are the semi-major and semi-minor axes of the synthesized beam at half maximum in arcseconds and $S(\nu)$ is the measured flux density at a given frequency (Fernández et al. 2013).

1.3 Continuum Emission

Other forms of radio emission comes in two forms. The first is thermal in nature. An example of this type of emission is free-free (bremsstrahlung) emission commonly found in HII regions (Condon & Ransom 2016). Free electrons moving past positive ions without being captured experience a change in velocity and thus emits radiation. On the other hand we have non-thermal processes. Electrons moving through magnetic fields experience a Lorentz force perpendicular to both the magnetic field and the direction traveled by the electron. This new tangential motion added to the particles initial trajectory results in the electron spiralling around the magnetic field line. The acceleration of the electron results in linearly polarised emission of radiation at radio wavelengths called synchrotron emission (Condon & Ransom 2016). A large portion of synchrotron emission in the universe come from active galactic nuclei. Relativistic jets produced by supermassive black holes in the center of these galaxies interact with magnetic fields in the ISM. In this thesis we are more interested in "normal" star forming galaxies. These objects also emit synchrotron radiation, but due to different mechanisms. When massive stars with masses greater than 8 $M_{\odot}$ eventually go supernova (Type II), the relativistic electrons which are accelerated by the outward blast of the supernova remnant (SNR) emit in the radio (Condon 1992). Since these are massive stars with short lifetimes, we can trace how many new stars have been formed in a galaxy from its continuum radio emission from SNRs. This is extremely useful, since radio wavelengths are not effected by dust. This gives us a direct way of measuring the star formation rate of galaxies via 1.4 GHz radio luminosity which is not effected by extinction processes. How this is done is discussed in §3.2.1.

1.4 LCBGs

Luminous compact blue galaxies, LCBGs, are a heterogeneous subset of starburst galaxies that are abundant at intermediate redshifts, but rare locally (Phillips et al. 1997). This makes them a very rapidly evolving population of galaxies and hence very good candidates for studying galactic

evolution as a whole. The first LCBGs were identified by surveys looking for faint quasi-stellar objects by Koo et al. (1994). These galaxies are traditionally defined according to the following criteria: they have a rest frame luminosity of $M_B < -18.5$ mag, a colour of $B - V < 0.6$ mag and an effective surface brightness of $SB_e(B) < 21$ mag arcsec^{-2} (Werk et al. 2004). These parameters make them overlap with various other galaxy types and it is important to distinguish LCBGs from these other objects. Faint blue galaxies, blue nucleated galaxies and compact narrow emission line galaxies (CNELGs) all fall under LCBGs as they are similar in terms of colour, size and star formation rates (Guzmán et al. 1997, Phillips et al. 1997). UV-Luminous Galaxies, defined to have a far-ultraviolet luminosity $\geq 2 \times 10^{10} L_{\odot}$, overlap with higher mass LCBGs (Heckman et al. 2005). Green Pea galaxies overlap with LCBGs in terms of morphology, luminosity, metallicity and stellar mass (Cardamone et al. 2009). These galaxies are small, rapidly evolving emission line galaxies which are bright in green wavelengths. LCBGs have also been suggested to be lower mass counterparts of Lyman Break Galaxies at lower redshifts (Guzmán et al. 2003). LCBGs are commonly confused with Blue Compact Dwarf galaxies (BCDs), although this is a completely separate class. BCDs tend to be less massive, less luminous and have a lower metallicity than LCBGs (Garland et al. 2004, Tollerud et al. 2009). Werk et al. (2004) found the average metallicity of their sample to have have near solar metallicities: $12+\log[O/H] \geq 8.4$, more than that of BCDs. Tollerud et al. (2009) found that the metallicity-luminosity relation for their sample of LCBGs agree with that of typical intermediate redshift galaxies. The relation between metallicity and compactness of these galaxies are thought to be important when looking at their possible evolutionary paths (Tollerud et al. 2009), but the same study showed no strong correlation between their size and oxygen abundance. This means that their evolutionary paths are likely to be varied as well.

Some studies split LCBGs into two different classifications. Around 60% of the sample in a study by Guzmán et al. (1997) were said to be HII-like since many of the properties of these galaxies resembled those of local HII galaxies. HII galaxies are very luminous galaxies undergoing intense star formation with spectra similar to those of HII regions. Both HII

galaxies and LCBGs are age-composite systems with a stellar populations spanning a wide range of ages (De Hoyos 2006), thus they have comparable star formation histories. The remaining 40% of the sample were classified as SB disk-like. These systems were much more evolved in terms of star formation and show similarities to local spiral galaxies and giant irregular galaxies. Guzmán et al. (2003) set out to measure the stellar masses of LCBGs at $0.4 < z < 1.2$. The total sample had a median mass of $M_* = 5 \times 10^9\ M_\odot$. This study also made distinction between HII-like and SB disk-like LCBGs. SB disk-like LCBGs tended to be more massive than HII-like ones with medians of $M_*(\mathrm{SB}) = 2 \times 10^{10}\ M_\odot$ and $M_*(\mathrm{HII}) = 5 \times 10^9\ M_\odot$. When compared to galaxies with luminosities similar to that of the Milky Way, LCBGs are about 10 times less massive at intermediate redshifts (Guzmán et al. 2003). Dynamical mass is the mass of a galaxy inferred from its rotation curve, which is a measure of a galaxy's velocity at a given radius. To compare dynamical masses in a sample, one has to make comparisons within the same radius. Garland et al. (2004) measured a range of $M_{dyn} = 8 \times 10^8 M_\odot$ to $3 \times 10^{10} M_\odot$ with a median of $8 \times 10^9 M_\odot$ within the effective radius. They found that the dynamical masses are consistent with low luminosity spiral and lower mass ellipticals.

LCBGs are starburst galaxies, meaning their star formation rates (SFRs) are much higher than the average SFR measured in other galaxies. LCBGs are likely significant contributors to the global star formation rate density (Guzmán et al. 1997), which makes this a particularly interesting property to track. Garland et al. (2005) calculated SFRs from a local sample of LCBGs by studying their infrared fluxes. They found them to range from 0.4 to 14 $M_\odot \mathrm{yr}^{-1}$ with a median value of 1.5 $M_\odot \mathrm{yr}^{-1}$. These values could be compared to those calculated from intermediate redshift LCBGs. Their specific star formation rates (their SFR normalised by their stellar mass) ranged from 1.1 to 6.6×10^{-10} yr^{-1} - similar to HII galaxies and much larger than that of normal spiral galaxies (Garland et al. 2005). Their total SFR seems to increase with redshift, as observed by Hunt (2017), with the average of their sample's SFRs at $z = 0.92$ being approximately 25 times higher than those at $z = 0.12$.

The intense star formation of LCBGs could be the result of their own

compactness or because of mergers/interactions with other galaxies. The morphologies of observed LCBGs, along with their velocity distributions, should shed some light on possible triggers of the starbursts. The question is whether these galaxies are in fact small, or merely very luminous starbursts at the center of larger disk galaxies. A sample of LCBGs from $z = 0.2-1.3$ was studied by Noeske et al. (2006) in order to investigate this. They found that around 90% of the galaxies in their sample were indeed small galaxies (with scale lengths less than 2 kpc). This suggests most are likely to evolve into small disk like or low-mass galaxies (Noeske et al. 2006). LCBGs are heterogeneous and thus differ a lot in morphology from each other. They are generally irregular or have a spiral structure. We show a selection of LCBGs in Figure 4. Local LCBGs also tend to have clumpy morphologies. A galaxy is classified as clumpy when it visually has three or more clumps (Garland et al. 2015). In the same paper Garland et al. (2015) also distinguishes between three types of local LCBGs: 1) those whose interaction with other galaxies and/or clusters trigger star formation (20%), 2) clumpy, spiral galaxies where smooth accretion is the main contributor to star formation (40%) and 3) non-clumpy, non-spiral, centrally concentrated galaxies (40%). In terms of kinematics, most LCBGs are rotating, with some showing distortion in their velocity fields (Gallego 2009, Rabidoux et al. 2018).

The differences in morphologies observed are likely due to the presence of companions, as is typical for starburst galaxies. LCBGs may interact with other nearby galaxies and this would have an effect on their star forming regions. Around 50% of the sample studied by Garland et al. (2015) had one or more optical companions that lie within 100kpc of that galaxy. In another study by Gallego (2009), 43% of the galaxies in their sample were found to have a companion. Clearly the presence of a companion has an effect on the star formation of these galaxies. Interestingly, LCBGs which are part of merging systems are in less common than one would think. Only 20% of the LCBGs in a sample observed by Garland et al. (2015) showed evidence of being the result of a merger. Similarly, the kinematics of 10% of the galaxies in the Gallego (2009) sample were likely the result of minor mergers with 5% showing evidence of major mergers.

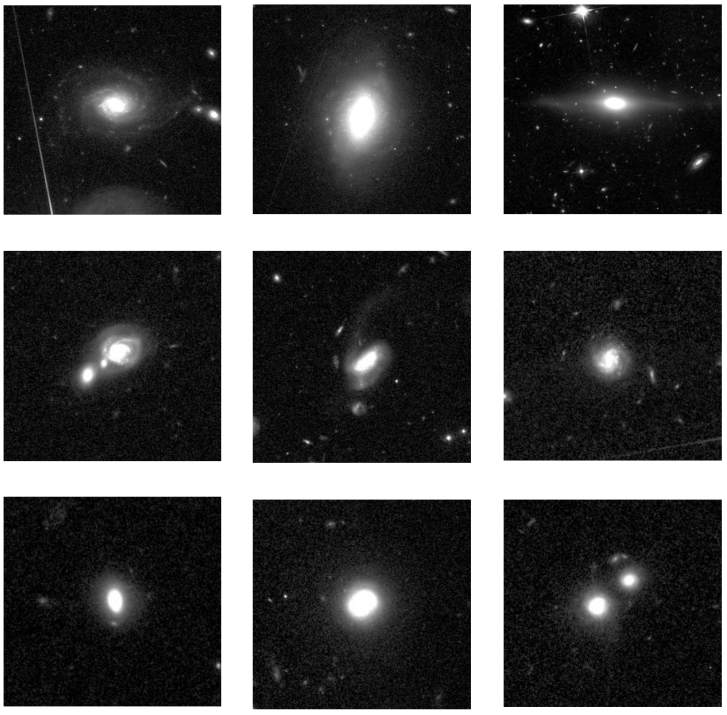

Figure 4: HST images of some of the closest LCBGs from our sample showing the variety of morphologies and properties present (Koekemoer et al. 2007).

LCBGs are more likely to be found in denser regions like clusters. They form around 50% of what is known as the Butcher-Oemler population. The Butcher-Oemler effect is the observation that the fraction of blue galaxies in the core of clusters increase with redshift. (Butcher & Oemler 1978). Their number density at intermediate redshifts increases by a factor of around 749 when observing clusters as apposed to field LCBGs (Crawford et al. 2011). Field and cluster number densities both rise with redshift in their study's sample. The field number density ranges from 1.2×10^{-3} Mpc^{-3} at $z = 0.5$ to 9×10^{-3} Mpc^{-3} at $z = 0.9$. For clusters, they measured a range of 1.62 Mpc^{-3} at $z = 0.55$ to 3.13 Mpc^{-3} at $z = 0.8$. The cluster environments are likely triggering the starburts. In a later study, Crawford. et al. (2014) found that cluster LCBGs have on average higher velocity dispersions than their field counterparts. Evidence of sub-clustering was also found, with LCBGs likely having velocity dispersion comparable to their nearest neighbours. Randriamampandry et al. (2017) compared their sample of cluster LCBGs to field LCBGs observed by Guzmán et al. (2003). The two groups were found to have quite similar mass distributions. What

stood out in terms of mass estimates was that for cluster LCBGs they measured a median of $M_{dyn}/M_* = 2.6$, but the field sample gave a median value of $M_{dyn}/M_* = 4.8$. These are comparable to cluster and field dwarf ellipticals. Hence, if LCBGs were to evolve into dwarf ellipticals, this ratio is set at the initial in-fall of the galaxy into the cluster. In terms of other parameters like SFR, size, luminosity and metallicity, field and cluster LCBGs are virtually the same (Crawford et al. 2016).

Moving on to lower redshift observables, LCBGs have been studied in the visual, near-infrared and radio wavelengths in local and intermediate redshifts in order to constrain theories on their evolutionary tracks. HI masses are measured to span the range of those in nearby galaxies along the Hubble sequence with a median $M_{HI} = 5{\times}10^9 \mathrm{M}_\odot$ and their gas richness range from $0.03 < M_{HI}/M_{dyn} < 0.2$ (Garland et al. 2004). These fractions range from those found in normal spirals (< 0.1) (Roberts & Haynes 1994) to very gas rich blue compact dwarfs (~ 3) (Van Zee et al. 1998). They also tend to have mass-to-light ratios smaller than normal galaxies in the local universe. It has been observed that HI emission tends to be centrally peaked along with optical emission and then continues to emit from an envelope further outward (Rabidoux et al. 2018).

From $z \sim 0.1$ to $z \sim 1$, the characteristic luminosity of LCBGs decreases by approximately 0.22 mag and the number density increases by a factor of 4. In that same range, the effective surface brightness increases by approximately $5.4 \times 10^{-3} h_{70}^{-3}$ Mpc^{-3} (Hunt et al. 2021). They make up around 42% of the luminosity density of galaxies with $M_B < -18.5$ at $z = 0.9$ (Hunt 2017). With less than 2% of the galaxies in the local universe being LCBGs, they are clearly a very rapidly evolving class of galaxies. The main challenge has been trying to find what they evolve into. LCBGs evolve at a faster rate than spirals, but not as fast as irregular galaxies (Hunt et al. 2021). There are two school of thought when it comes to what LCBGs may evolve into. The one theory is that they may be the progenitors of the bulges of massive local spiral galaxies (Phillips et al. 1997, Hammer et al. 2001). This would likely the be case for SB disk-like LCBGs. Another theory is that they evolve into lower mass elliptical galaxies, because the luminosities and surface brightness of HII-like LCBGs

are likely to fade to be comparable to dwarf ellipticals (Koo et al. 1994). A critique of this is that LCBGs are rotationally supported, meaning it is unlikely that they would lose a sufficient amount of their rotation to be comparable to dEs.

What LCBGs will eventually become is still an open question. If we wish to understand the galactic evolution of galaxies between $0 < z < 1$, LCBGs offer a great laboratory because of their rapidly evolving nature.

1.5 Aims

Our primary aims are to use HI spectral line data, as well as L-band continuum data (§2.1 and §2.2) to quantify how Luminious Compact Blue galaxies are observed to evolve between $0 < z < 1$. We aim to directly detect neutral hydrogen at local redshifts and indirectly detect HI at intermediate redshifts via stacking techniques (§3.1.2). This would paint a picture of how the HI content of LCBGs evolved over 9 billion years of lookback time. This is of course determined by how efficiently hydrogen is being converted into stars. Hence, we also aim to measure the star formation rates of LCBGs (§3.2.1) by means of their 1.4 GHz luminosities, which gives an extinction-free estimate of the SFR of star forming galaxies. By quantifying the changes of their SFRs normalised by their stellar masses over cosmic time, we can directly compare the evolution of LCBGs to other starburst galaxies. Finally, we would like to take all we have observed and see what it tells us about the fate of LCBGs as they evolve to the present day.

1.6 Outline of thesis

In this chapter, we started by giving a broad overview of galactic formation and evolution as we understand it today. We describe how galaxies are classified, as well as how they interact with each other and evolve morphologically. We then look deeper into the evolution of HI in stellar systems as well as how we observe star formation rates to evolve over cosmological time. We describe the mechanism that triggers HI emission and how we

measure it as well as other processes that emit in the radio and how they are useful. We finally give a description of LCBGs and what we currently understand about them. In Chapter 2 we give a description of the data surveys used in this work, as well as the sample selection of galaxies that we studied. In Chapter 3 we discuss our main findings. We describe the techniques used to detect HI in our data and discuss the properties of our direct detections. We then describe how we went about stacking our data to measure HI at higher redshifts and what we found. Lastly, we discuss how we went about studying the evolution of SFRs in LCBGs. In Chapter 4 we summarise the main outcomes of this thesis and discuss what we can can do to further investigate LCBGs in the future. For all calculations in this thesis, we assume $H_0 = 70$ km s^{-1} Mpc^{-1}, $\Omega_M = 0.3$ and $\Omega_\Lambda = 0.7$ in a flat ΛCDM model.

Chapter 2

The Data

To do excellent science, we require excellent data and to effectively study our set of galaxies, we require galactic surveys that are large enough to contain a representative sample. Radio interferometry has come a long way and the VLA and MeerKAT are proof of how far we have come. In this chapter, the data used in this thesis is described, as well as a brief history of the most recent science done with them.

2.1 The CHILES survey

The COSMOS HI Large Extragalactic Survey (CHILES) is a neutral hydrogen deep field survey done by the Karl G. Jansky Very Large Array in its B-configuration. The field covers a redshift range of $0 < z < 0.5$ (947 to 1420 MHz) and is situated in the COSMOS field, making it first multi-epoch survey of its kind to continuously observe HI in this redshift range (van Gorkom et al. in prep, Luber 2022). COSMOS is a well-studied patch of sky, rich with auxiliary data across many wavelengths spanning X-ray to radio (Koekemoer et al. 2007). It is situated in region devoid of gas from the Milky Way and with minimal stars. It is also free from major continuum sources. In the L-band, the VLA's primary beam has a full width at half maximum given by $\theta_{PB} = 45/\nu_{GHz}$. This results in a beam size of $47.5'$ at 947 MHz and $31.7'$ at 1420 MHz.

The CHILES field was first observed in a pilot survey in 2011. The survey took place in a redshift range of $0 < z < 0.193$ (Fernández et al.

Key Parameters	
Pointing	$10^h01^m24^s + 02°21'00''$
Frequency range	947 MHz - 1420 MHz
Pixel size	$2''$
Image size	1200×1200 pixels
Integration Time	1027 hrs
Observations	5/10/2013 - 11/04/2019
Spectral Resolution	125 kHz
Synthesized Beam (FWHM)	$9'' \times 9''$

Table 1: Summary of properties of our final CHILES cube.

2013). This was done during the upgrade of the VLA's wide band L-band receivers and correlator to have the potential of observing in the continuous range of $0 < z < 0.45$. The main aim of this study was to test the array's capabilities with the goal of a deep field observation in the future. They detected 33 galaxies in 50 hrs of observing time. Analysis of the radio frequency interference (RFI) showed it was mainly present in baselines less than 2 km. This proved the B-configuration of the VLA to be optimal, since 70% of its baselines are larger than 4 km. The longest baseline in this configuration is 11.1 km. The furthest confirmed direct HI detection was found by Fernández et al. (2016) where they detected the galaxy COSMOS J100054.83+023126.2 at $z = 0.376$. This was done using the first epoch of CHILES data (178 hrs) and showed the luminous infrared galaxy possibly interacting with a companion. This marked first study of atomic and molecular hydrogen at intermediate redshifts and solidifies CHILES as an optimal data set for studying how neutral hydrogen evolves over higher redshifts. Hess et al. (2019) did a study of two redshift ranges that were heavily effected by RFI: $0.108 \leq z \leq 0.127$ and $0.162 \leq z \leq 0.183$. Proving that CHILES can produce good quality data in these regions, they detected 16 galaxies and studied their properties in relation to their environments. Nearby galaxies have further been observed using the first epoch data. The data seems to agree with known scaling relations (Blue Bird et al. 2020). Most findings to date however have been done using the first 178 hr data. This project is among the first to do analysis on the full data set.

The final HI cube was produced with a pixel scale of $2'' \times 2''$ and an original spectral resolution of 15.625 kHz, which was smoothed to a reso-

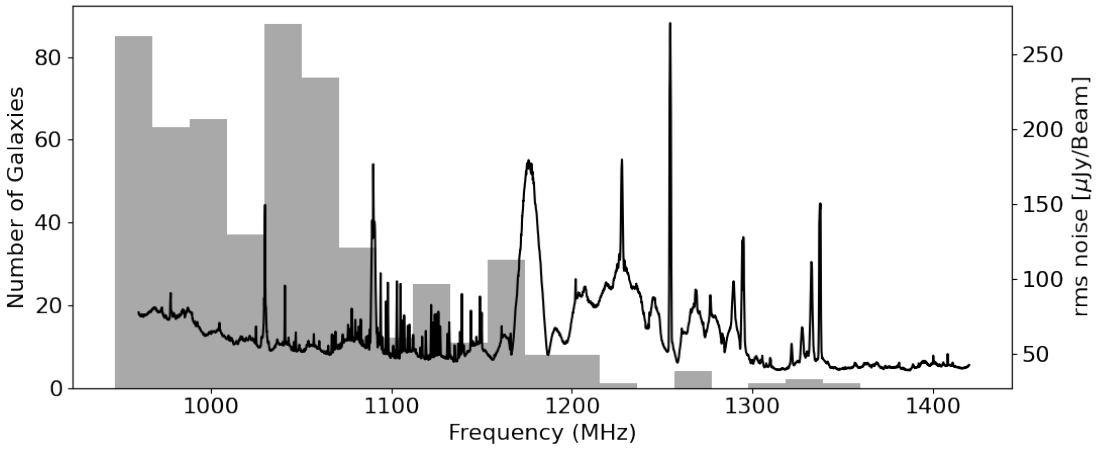

Figure 5: The RMS noise over the full frequency range of the CHILES cube. This histogram indicates the distribution of LCBGs in frequency bins throughout the cube.

lution of 0.125 MHz which corresponds to $\approx$ 25 km/s wide channels (van Gorkom et al. in prep, Luber (2022)). The cube is $2400'' \times 2400''$ in size with a synthesized beam size of $9'' \times 9''$. The beam size was smoothed to be a constant size over the entire frequency range. The cube has an average noise of 63.5 μJy/Beam per channel, but we see a general increase in noise between 1160 MHz and 1300 MHz (see Figure 5). We also observe spikes in noise at around 1030 MHz, 1090 MHz and 1333 MHz. The main properties of the final cube are shown in Table 1.

2.2 CHILES Con Pol

Alongside CHILES, the VLA also set out to create an L-band continuum image of the same field (see Figure 6). This is known as the CHILES Continuum Polarization survey (CCP). The observations were done simultaneously with CHILES resulting in a 1000 hr deep field 1.4 GHz continuum data with a total bandwidth of 512 MHz. The imaging was done with polarisation. With a synthesised beam resolution of $4.5'' \times 4''$ and a RMS noise of 1.3 μJy per beam, this survey marks the most sensitive image of this frequency range to date (Luber 2022, Luber et al. in prep, Gim et al. in prep). CHILES Con Pol is thus very well suited to detect objects in the redshift range that we are interested in.

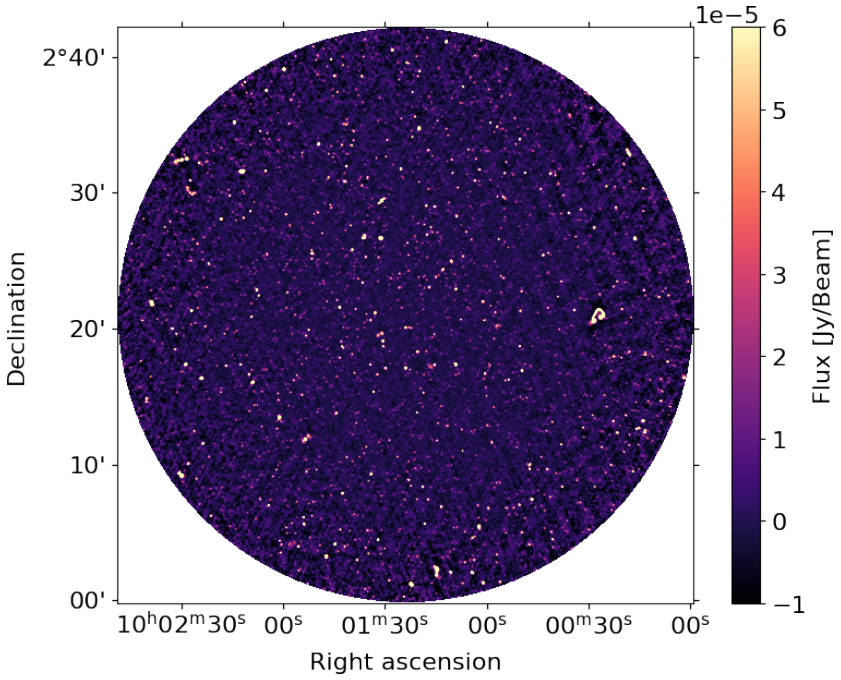

Figure 6: The radio continuum image of the CHILES Continuum Polarization survey at 1.4 GHz.

2.3 Our galaxy catalog

COSMOS, being such a well studied region, offers many surveys on the galaxies within it. The LCBGs in our study were identified from within COSMOS survey, but was reprocessed by the Galaxy and Mass Assembly survey (GAMA) (Driver et al. 2011). GAMA utilised an ensemble of ground-based telescopes to produce a multi-wavelength survey of over 300 000 galaxies to study galaxy evolution as well as test our current cosmological theories. The survey covers many areas of the sky. The survey region centered in COSMOS is labeled G10 and contains $\approx$ 18000 sources with photometry covering UV to FIR (Davies et al. 2015). In order to identify LCBGs, the B-band luminosity, colour and surface brightness of the galaxies in this survey was calculated by Hunt (2017). We use this selection of LCBGs for our analysis. In Figure 7 we can see how the LCBGs are identified from these three parameter cutoffs. The reshifts that we used also come from this data set. We used spectroscopic redshifts originally measured in the zCOSMOS survey (Lilly et al. 2007) as well as the PRIMUS survey (Coil et al. 2011), but which were reproduced by the GAMA pipeline

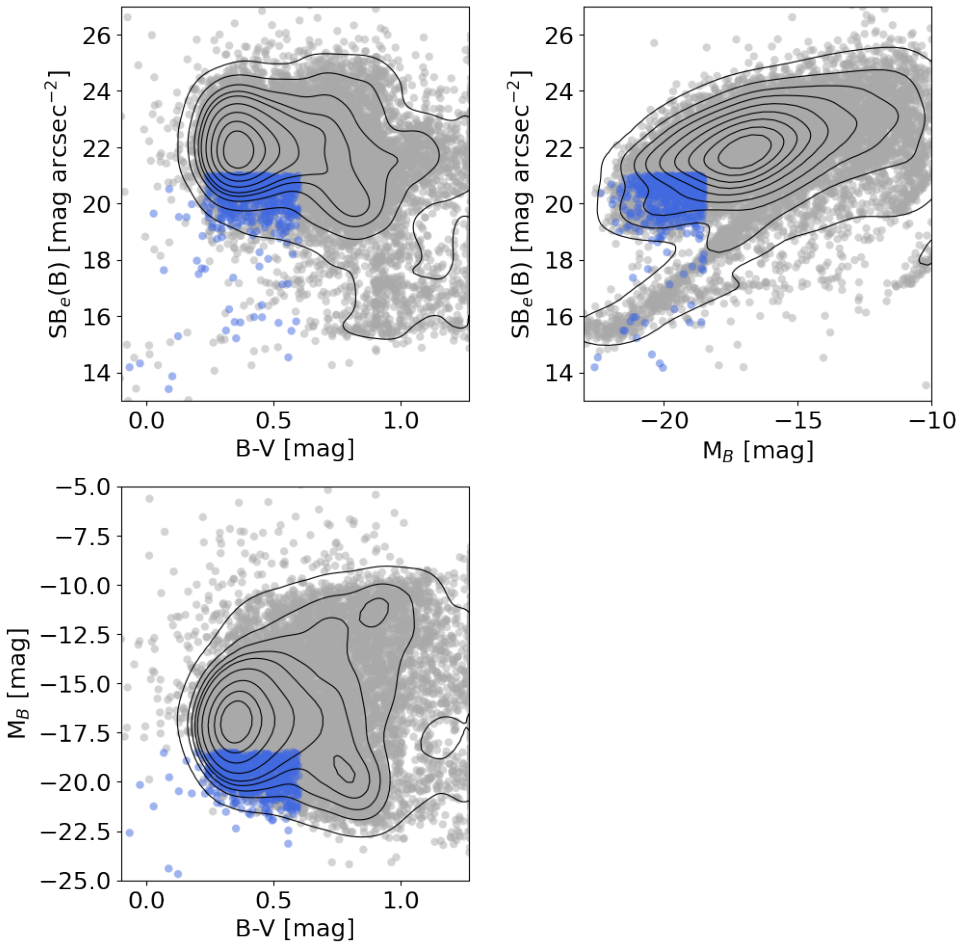

Figure 7: Our full catalog of LCBGs (blue) identified from all galaxies in the G10 region (gray) via their color ($B-V$), B-band magnitude (M_B) and surface brightness ($SB_e(B)$). We see the LCBGs populating the one corner of the parameter space. In each sub-figure, the grey points in the LCBG quadrant represent those galaxies that do not meet the third criteria. The contours represent the number density of galaxies in the parameter space.

which yielded better spectra.

The stellar masses used for the galaxies in our sample was taken from the COSMOS2015 catalog (Laigle et al. 2016). COSMOS2015 contains photometric redshifts and stellar masses of galaxies in the COSMOS field up to $z \approx 4$. We cross-matched the two catalogs and we were left with a final sample of LCBGs of which we have known stellar masses, which can be seen populating the higher mass end of the blue cloud in Figure 8. All cross-matching was done via each galaxy's COSMOS2008 ID. We see that most of the LCBGs in our sample have $M_* > 10^9$ M$_\odot$ and $B - V > 0.2$ mag, with a few exceptions of lower mass and very blue LCBGs.

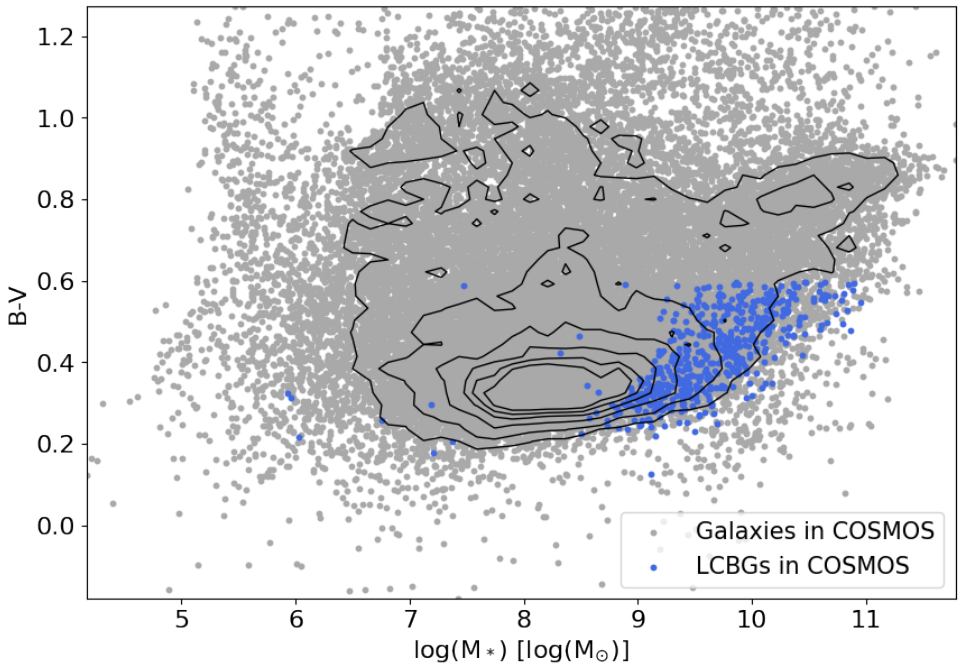

Figure 8: Colour vs stellar mass plot showing our sample of LCBGs laying in the high mass end of the blue cloud. The contours represent the number density of galaxies in the parameter space.

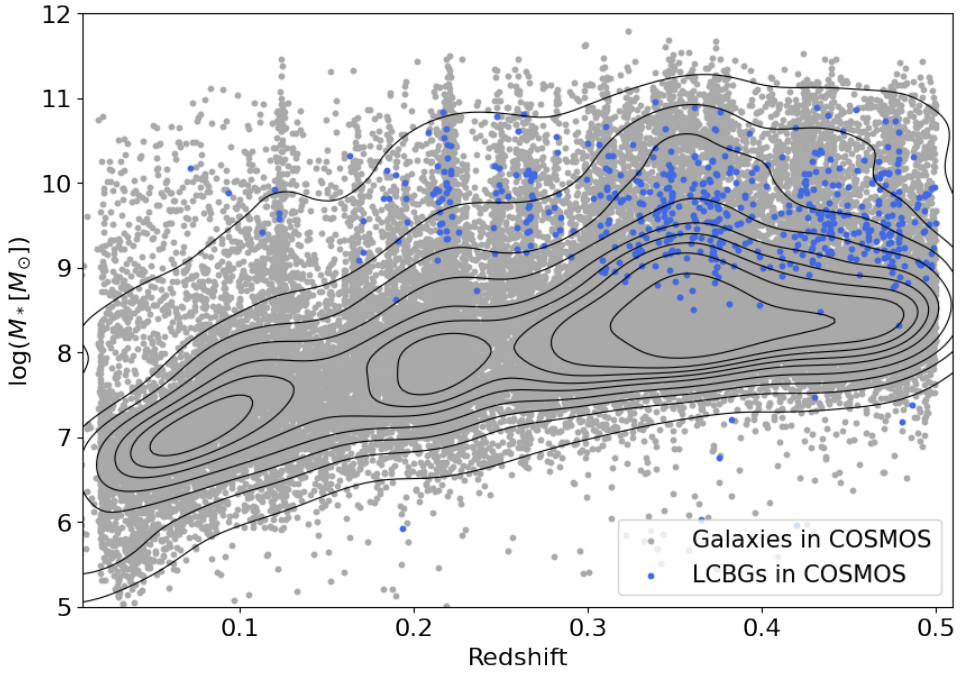

Figure 9: Redshift vs stellar mass distribution for our sample of LCBGs. The contours represent the number density of galaxies in the parameter space.

We show the redshift distribution of our catalog in Figure 9. LCBGs are much more common at higher redshifts. The spread in the stellar masses of LCBGs also seems to be consistent throughout all redshifts for $z > 0.2$.

Chapter 3

Analysis and Results

3.1 The evolution of HI mass

3.1.1 Direct detections

The first thing we set out to do was look for direct detections of LCBGs throughout the entire spectral cube. We made use of the HI Source Finding Application, SoFiA 2 (Serra et al. 2015, Westmeier et al. 2021). This application makes use of a 'smooth and clip' algorithm to find sources within the noise of the cube. The algorithm first performs Gaussian smoothing on the spatial dimensions and boxcar smoothing in the spectral dimension of the cube. If the flux of the smoothed data is above a certain threshold with regards to the rms, it is included in a mask of a possible detection. This process is continuously repeated, looping through combinations of spectral and spatial kernels until the algorithm is satisfied that all pixels with notable flux has been masked. A 'friends of friends' algorithm is then implemented to link masked pixels to form part of one single HI source. Finally SoFiA 2 measures the reliability of the detections produced and only keeps the ones that fits the requirements of the user.

Since we already had a catalog of LCBGs, all we required was a final mask of all possible detections, which we could cross-match to the coordinates of the galaxies in our list. We wanted to be absolutely certain that sources picked up at these select coordinates were indeed real detections so our reliability threshold was set to 90%. SoFiA 2 produced a large

mask cube with the same dimensions as the original spectral line cube. To efficiently search through the individual detections to see whether there are any matches with our source list, we made use of iDaVIE-v, a virtual reality data visualisation and rendering (Comrie et al. 2021). The source mask is loaded into iDaVIE-v along with the catalog of LCBG coordinates and redshifts. The mask is then rendered in virtual reality in the form of voxels within the RA-DEC-redshift parameter space. The LCBGs are rendered in the same three dimensional space as points. The data is viewed by means of a virtual reality headset and can be moved and inspected via two remote controllers. We proceeded to search the space for locations where the mask overlaps with a point. If an overlap is found, it would imply that SoFiA 2 has detected HI emission around the coordinate of an LCBG. We found three of these occurrences. The central coordinates of these three detections as well as the coordinates of the three LCBGs were recorded for further inspection.

We extracted spectra from the original cube within an aperture of the size of this region. From these maps and spectra we could determine if these were indeed direct detections. We show the spectra in Figure 10. A 1st order polynomial fit was done and subtracted from the spectra in Figures 10a and 10b. In these spectra we clearly see two detections. Figure 10a shows a single peak and Figure 10b shows a clear double peak profile. The velocity width in Figure 10a at 20% peak emission is $W_{20} = 317$ km s^{-1}. The detection in Figure 10b has a slightly smaller width of $W_{20} = 211$ km s^{-1}. A 2nd order fit was performed and subtracted in Figure 10c, because the peak occurs adjacent to a noisy region in the cube. We observe emission at a much smaller SNR, but we believe it to be a detection nonetheless, because of heightened emission in consecutive channels around where we expect the HI line. For this peak we measure $W_{20} = 343$ km s^{-1}. We note that there are two sources roughly at the same position and redshift, one being an LCBG and the other one not. The emission we see in this region could be coming from both of these together. The locations of these two sources are shown in Figure 10c.

For each individual detection, we produced a moment 0, 1 and 2 map from data within the masked region. These are shown in Figures 11, 12

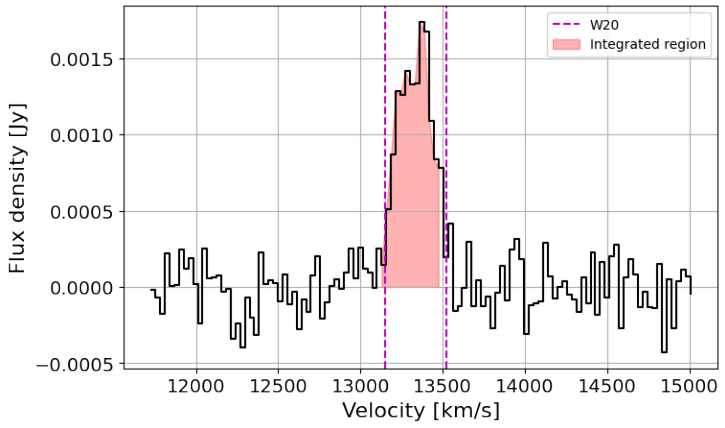

(a)

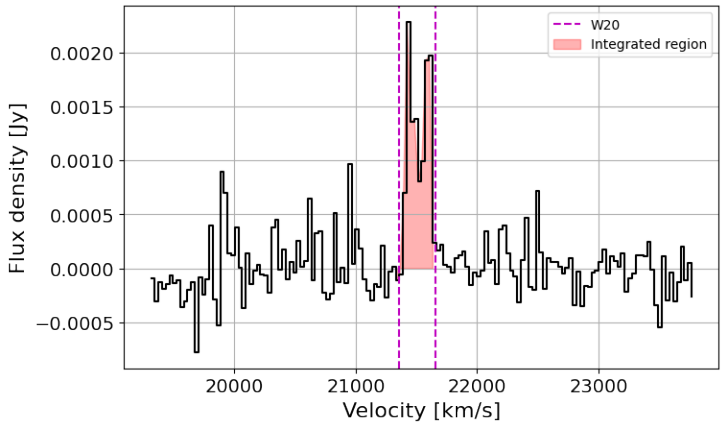

(b)

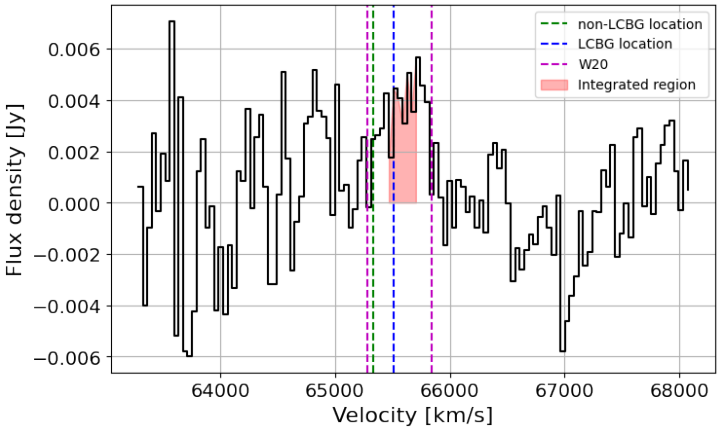

(c)

Figure 10: The baseline-corrected spectra extracted from the three directly detected LCBGs. The width of each line at 20% peak emission is shown by the dashed purple lines. The filled in area shows the region used to calculate the integrated flux, which corresponds to the masks created by SoFia 2. In (c) we indicated the location of the two sources that could be responsible for the HI emission.

z	α J2000	δ J2000	$\mathbf{D_L}$ Mpc	$\mathbf{S_{int}}$ Jy Hz	$\mathbf{M_{HI}}$ $10^9 M_\odot$	$\mathbf{W_{20}}$ km s^{-1}	**S/N**
0.045	150.23	2.40	199.34	1782.36	3.53 ± 0.06	317 ± 26	23.25
0.072	150.27	2.51	325.13	1435.05	7.55 ± 0.23	211 ± 26	13.50
0.219	150.40	2.52	1084.97	3467.79	202.70 ± 18.94	343 ± 26	5.01

Table 2: Measurements of the directly detected LCBGs. D_L is the luminosity distance of the galaxy. $S_{\rm int}$ is the integrated flux density. The uncertainty in W_{20} is one channel width. S/N is the integrated signal to noise ratio of each peak.

and 13. Looking at the first detection in Figure 11, which lies at $z \approx 0.045$, the HI column density contours in Figure 11a correspond nicely with the optical HST image of the LCBG. We could be observing some disruption in the gas with respect to the stellar component towards the northern part of the image. The velocity distribution shown in Figure 11c shows even rotation throughout the gas. Figure 11b is a position-velocity diagram taken along the gray line in the velocity map, placed along the major axis. We see a clear indication of rotation. The moment 2 map in Figure 11c shows generally even velocity dispersion, except for two small regions towards the south of the cloud.

In the second detection at $z \approx 0.072$ in Figure 12, we again see that the HI contours surrounds the stellar component with the major axes approximately equal. Again the velocity map is fairly uniform. The PV diagram shows much a more prominent indication of rotation with the approaching and receding components clearly defined. The moment 2 map shows an increase in velocity dispersion towards the center of the map. We note that these features are barely larger than the beam, so we are likely just observing beam smearing artifacts.

The furthest detection, at $z \approx 0.219$ (Figure 13), peaks towards the northeast of the LCBG's stellar component. The optical source in the center of the contours is not an LCBG, but is at approximately the same redshift. We are likely measuring HI present in both these sources. The optical locations of both these sources are shown in Figure 10c. We can make out a slight velocity gradient in the moment 1 map. When taking a PV diagram along that gradient, we see what appears to be a rotation curve, further confirming that this is indeed a detection. The moment 2

map shows variation throughout the source, but this is likely due to the source being only slightly larger than the beam itself. Pixel by pixel SNR maps of all three detections are shown in Figure 14. This gives us more confidence in the morphology of our detections and shows us the peak value of each detection is at least four times greater than the RMS around the sources in each case.

We measure HI masses from the three detections by integrating over the velocity range of the mask generated by SoFia 2 for each detection. Since our cube is split into channels of equal frequency, we integrate with respect to $d\nu$. We calculate the luminosity distances to each of the galaxies from their redshifts and then proceed to calculate M_{HI} using equation 1.11. Our results are shown in Table 2. The uncertainties in our mass estimates are calculated from the uncertainty in our flux calculations as done in Chandra et al. (2004). We calculate the off-line RMS and add it in quadrature to 10% of the peak flux value:

$$u(S) = \sqrt{S_{RMS}^2 + (0.1S_{peak})^2} \tag{3.1}$$

The HI mass of the higher redshift is clearly too large to belong to one galaxy. This suggests that what we are seeing is the combined HI gas from the LCBG interacting with the non-LCBG in the center of the contours.

3.1.2 HI Stacking

The highest redshift, direct HI detection from a single galaxy is at $z = 0.376$ (Fernández et al. 2016). Detecting HI at these redshifts is difficult, hence we frequently have to implement a method called stacking. This can only be implemented when the spectroscopic redshifts of sources that are likely to emit the 21 cm line are known. The method used to do this is generally known as 'spectrum stacking' (Zwaan 2000, Chengalur et al. 2001). What it involves is measuring the spectrum of the source at the coordinate and redshift where we expect it to be. This is repeated for many sources. Some spectra might show a detection at the redshifted frequency of the galaxy, but others might not. The spectrum is then shifted according to the source's known redshift. These aligned spectra are then combined, or stacked, in the form of a weighted average in order to raise the signal to

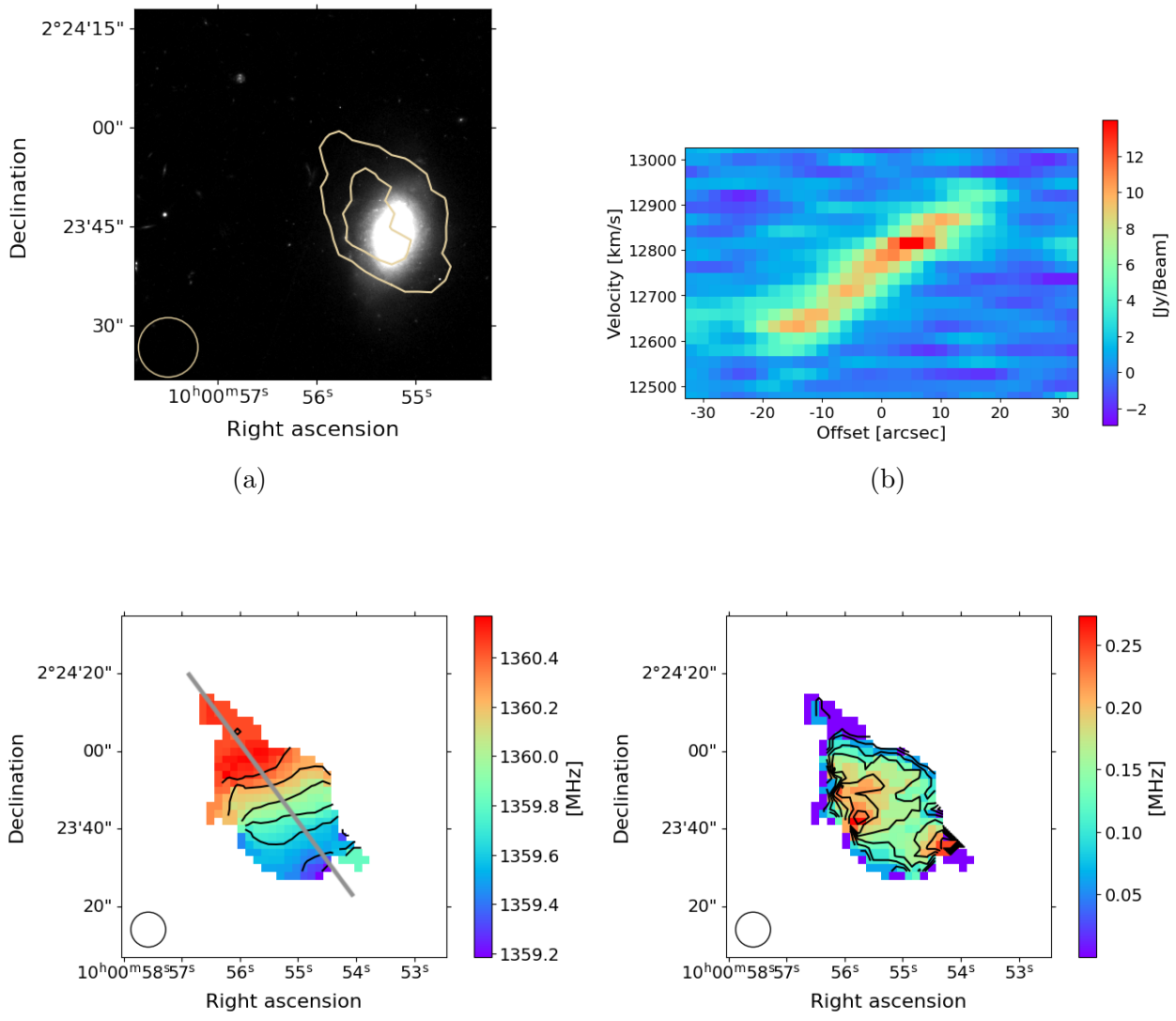

Figure 11: Moment maps of the direct detection of a LCBG at $z \approx 0.045$. (a) HI column density contours overlaid on top of an optical HST image. The contours represent 2σ and 3σ with $\sigma = 81$ Jy/Beam km/s. (b) A position-velocity diagram taken along the major axis of the radio emission. (c) A moment 1 map showing the distribution of wavelengths emitted from the radio data. The gray line indicates the cut along which the PV diagram was created. (d) A moment 2 map depicting the dispersion in the emission.

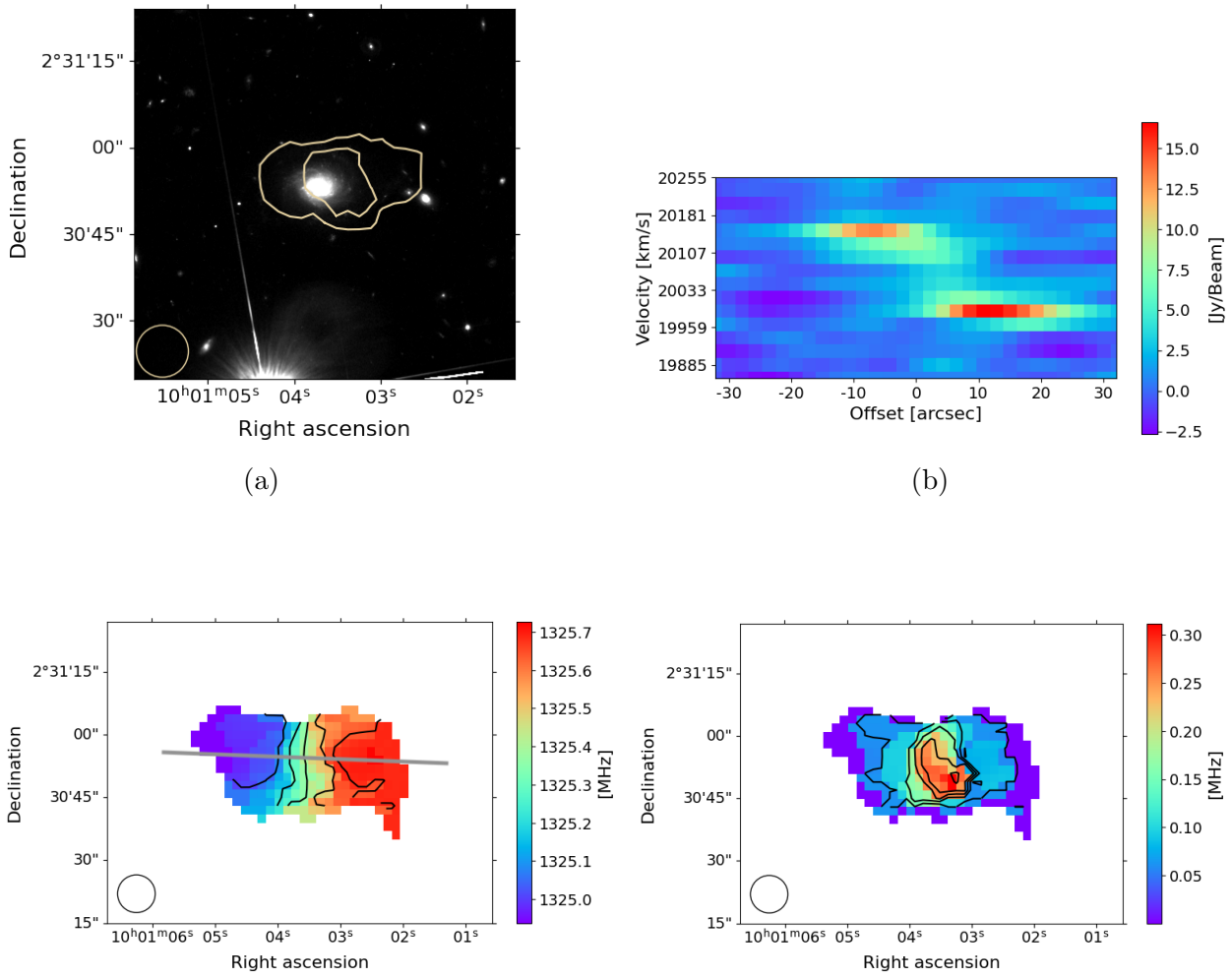

Figure 12: Moment maps of the direct detection of a LCBG at $z \approx 0.072$. (a) HI column density contours overlaid on top of an optical HST image. The contours represent 2σ and 3σ with $\sigma = 57$ Jy/Beam km/s. (b) A position-velocity diagram taken along the major axis of the radio emission. (c) A moment 1 map showing the distribution of wavelengths emitted from the radio data. The gray line indicates the cut along which the PV diagram was created. (d) A moment 2 map depicting the dispersion in the emission

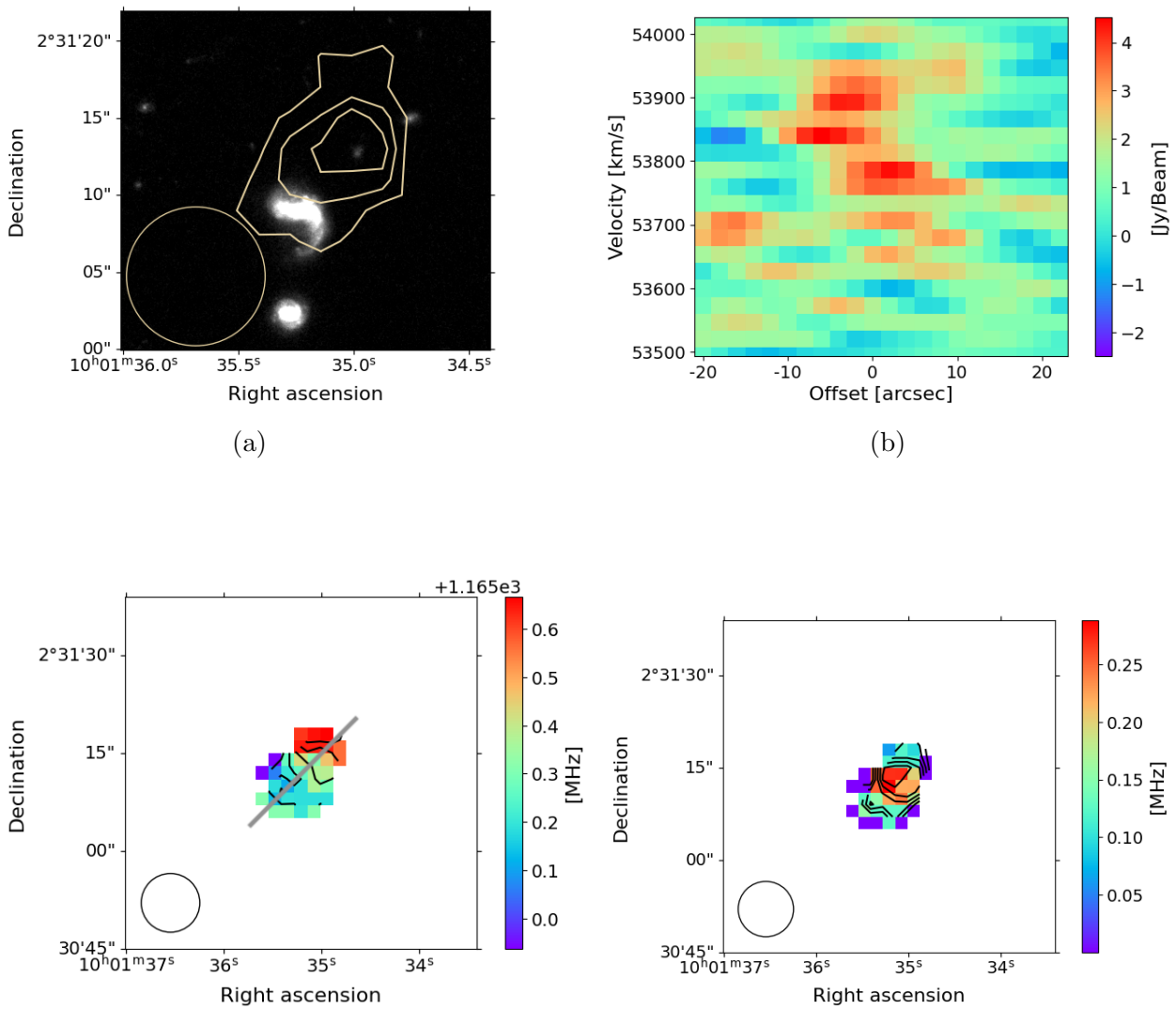

Figure 13: Moment maps of the direct detection of a LCBG at $z \approx 0.219$. (a) HI column density contours overlaid on top of an optical HST image. The contours represent 1σ, 2σ and 3σ with $\sigma = 33$ Jy/Beam km/s. (b) A position-velocity diagram taken along the major axis of the radio emission. (c) A moment 1 map showing the distribution of wavelengths emitted from the radio data. The gray line indicates the cut along which the PV diagram was created. (d) A moment 2 map depicting the dispersion in the emission

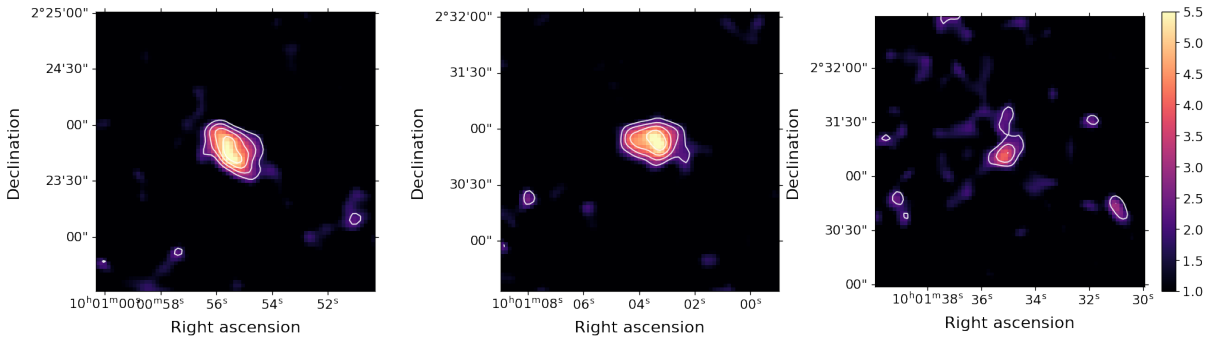

Figure 14: Signal to noise ratio maps for our three direct detections. The detections increase in redshift going from left to right. The contours represent a SNR of 2, 3, 4 and 5 respectively. Pixel values of 1 and lower are saturated in the color scale.

noise (Delhaize et al. 2013). In theory, if the noise is truly Gaussian, it should average out around zero. The signal on the other hand should be amplified. This way, we can measure a spectrum that is representative of the entire sample of galaxies. If we see a peak with a high enough integrated signal to noise and a believable width, we have a stacked detection. This spectrum can then be analysed as any normal detection would, with the only exception being that any values calculated from it, is now the mean of the sample. This technique was first shown to be successful to measure the average properties of field galaxies by Lah et al. (2007).

The method we used to stack LCBGs is a slightly altered approach called 'cubelet stacking' (Chen et al. 2021*a*). Instead of extracting a spectrum around each individual source, a small region around the source is extracted in the form of a sub-cube. These cubelets are then aligned such that the right-ascension, declination and redshift of the center of each source overlaps. The cubelets are then stacked and a spectrum is extracted from the stacked cube. Along with the stacked sources, point spread function (PSF) cubelets are also stacked. The reason for using this approach as opposed to standard spectrum stacking, is that sources should theoretically be resolved throughout the entire cube (Luber 2022). Our method follows that as described in Chen et al. (2021*a*). They argue that cubelet stacking results in a more accurate stack because we can perform a deconvolution of the stacked cube via a stacked PSF cube. This in turn results in more accurate flux and mass measurements. Our stacking procedure was as follows:

1. From an input source list with known coordinates and spectroscopic redshifts, we extract cubelets of 64 × 064 pixels and a width of 76 channels, or approximately 9.5 MHz, with the source exactly at the center of the cubelet. Sources that lie at the edges of the cube are removed prior to the extraction. This is because the cubelets which we extract around each source have to fit within the cube itself. We only extract sources that lie at least 32 pixels (half the size of a cubelet) away from the edge. This applies spectrally too, i.e. at least 38 channels from the edge.

2. The primary beam correction factor at the point of each source is calculated. The primary beam attenuation depends on the frequency of the emission: $\theta_{PB} = 45/\nu_{GHz}$, where θ_{PB} is the FWHM of the VLA's primary beam. A Gaussian primary beam is a good approximation for the real one (*VLA Observational Status Summary* 2024). From this we can infer the Gaussian width of the primary beam: $\sigma = \theta_{PB}/2\sqrt{2\ln 2}$. The correction factor at a given position in the beam is thus:

$$\beta = (e^{\frac{R^2}{2\sigma^2}})^{-1} \tag{3.2}$$

   where R is the distance from the beam center in arcminutes.

3. The cube is in units of Jy/Beam. This is converted to luminosity density per beam with units ($\mathrm{JyBeam^{-1}Mpc^2}$) by calculating the galaxy's distance from its given redshift.

4. Stacking is a weighted averaging process. The weights for each cubelet is calculated as:

$$w_i = \frac{1}{\sigma_i^2} \tag{3.3}$$

   where σ is the standard deviation of the cubelet. This weight slightly increases the SNR of the stacked spectrum. The cubes are then stacked as follows:

$$\langle S \rangle = \frac{\sum_{i=1}^{n} S_i w_i}{\sum_{i=1}^{n} w_i} \tag{3.4}$$

where S_i represents a single cubelet and w_i is its associated weight.

5. In order to do cubelet stacking, we also need a cube of the data's point spread function over the entire frequency range of the cube. A cubelet of the PSF is produced along with the source cubelets by cropping the spectral axis. The PSF cubelets are then stacked in a similar fashion.

6. The stacked cube is the cleaned using the Högbom cleaning algorithm (Högbom, 1974) and the stacked PSF cube.

7. A spectrum is then extracted from the center of the cubelet in a region of $14'' \times 14''$. Channels that show emission are identified. A 2D polynomial is fit to the off-emission channels and subtracted off if necessary. A stacked detection is deemed successful if the emission is centered at 1420 MHz with a high enough integrated signal to noise. We also inspect the noise around the integrated region by generating a moment 0 (HI column density) map over the channels with emission.

3.1.3 HI simulations

In order to make sure that our stacking process will be able to correctly search for a signal embedded in noise, we decided to simulate HI sources in a cube and perform our stacking technique on these sources. To do this, we first produced a cube of 760 channels and 640×640 pixels, representing approximately $22' \times 22'$ in the sky. It was filled with normally distributed noise. We then performed a convolution on the data with a Gaussian beam which had the same size as that of our CHILES cube: a FWHM of 4.5 pixels. This ensured that there were no discernible structures in the noise smaller than than this scale. What was left was to populate the cube with sources. A single source was modeled to have an intensity that drops off according at a Gaussian distribution in both the spatial directions as well as spectrally. Spatially our sources were set to be symmetric two-dimensional Gaussians with a size resembling that of a typical HI detection. Spectrally, the Gaussian width was set to resemble a typical HI line width that we would expect to observe in our data (we chose 8 channels at FWHM). Sixty of these sources were then embedded at random locations throughout the cube. The peak intensity of each of these sources was set to be lower than

the spread of the noise, so as to simulate sixty 'non-detected' sources. If our stacking procedure worked correctly, our final stacked spectrum should result in the average source peak surrounded by noise which has scaled down by $\sqrt{N}$, where N is the number of galaxies in our stack. The random sources are generated along with coordinates and redshifts which would lie in the original CHILES cube. We use the coordinates to extract cubelets around the sources and stack them exactly as we would with real data. This simulated cube is of course already 'cleaned', hence we omit the Högbom cleaning of the stacked cube. What we found was that the stacked spectrum did indeed show what we expected and that the noise scaled correctly. This assured us that our technique was adequate and we were ready to attempt stacking on our data.

3.1.4 Stacking results

Before we began to stack LCBGs, we had to look at the properties of our data cube in order to determine the optimal bins in which to stack. If we look at Figure 5, we coincidentally observe the number of LCBGs drop at around the same frequency range where the noise in the cube increases. Ideally we would like to a large enough sample of galaxies in our stack for it to be statistically significant, while simultaneously avoiding noisy regions in our cube. We chose to stack over the entire spatial extent of the cube to favour larger stacks. Our general procedure after we performed a stack was the following: We extract an integrated spectrum from the central square region of the stacked cubelet with a fixed size of $14'' \times 14''$ and then smooth the spectrum to a resolution of ≈ 50 km/s for a higher SNR. We then produce a moment 0 map over the channels which show emission. If no spectral detection is seen we create the map over channels spanning a velocity width of 227 km/s centered at the rest frequency of the stacked galaxies. This is the average W_{20} linewidth measured from a sample of local LCBGs by Garland et al. (2004) and would allow us to still inspect the moment map. We would then inspect the stacked spectrum as well as the moment 0 map to see whether we observe a detection both spectrally and spatially.

As a first trial, we decided to do one large stack of galaxies between

$940 < \nu < 1300$ MHz. This stack of 396 LCBGs, shown in Figure 15a, resulted in a detection with an integrated signal to noise ratio of 5.93. The right panel of Figure 15a shows a clear detection in the center of the stacked cubelet. This is a clear indication that we have detected neutral hydrogen in this redshift range. Next, we decided to exclude some of the noisier channels from our stack. We do the exact same procedure, but now between $940 < \nu < 1160$ MHz (354 galaxies). This stack is shown in Figure 15b. Again we see a clear detection (the integrated S/N is > 3). This proved that our detection was indeed of HI and not an artifact of noisy channels. From the stacked spectrum we could calculate $\int D_L^2 S(\nu) d\nu$, convert to units of JyMpc^{2}Hz and find the average M_{HI} of the galaxies in that sample using equation 1.11. All calculated masses are listed in Table 3. Since our primary goal is to trace the evolution of HI across redshift, we split this range into two bins of equal frequency width. We decided to bin in terms of frequency, since that is how the cube's channels are defined. We thus had two samples of LCBGs, each between $940 < \nu < 1050$ MHz (227 galaxies) and $1050 < \nu < 1160$ MHz (127 galaxies). When we stack the galaxies in these bins, we began to notice that we start losing detections. In the lower redshift bin shown in Figure 16a we see no evidence of a detection. We do however see a detection in Figure 16b, at a higher redshift. This detection has an integrated S/N of 4.73 and the largest positive peak occurs where we would expect a detection. We can also see what could be a detection in the center of the moment map. The central emission is accompanied by other bright spots in the outskirts of the map. When taking point spectra at these locations we observe bright emission in only single, detached channels, leading us to believe they are only imaging artifacts arising from the cubelets used in the stack. We can still measure a upper limit for the HI mass, σ_{HI}, from the non-detection. From equation 1.11 we can derive:

$$\sigma_{HI} = 49.8 D_L^2 \sigma_S d\nu \sigma_{SNR} \tag{3.5}$$

$D_L^2 \sigma_S$ represents the error in the cubelet in luminosity density units. This is calculated by resampling regions within the cubelet with sizes similar to that in which we would extract a stacked spectrum. $d\nu$ is the width of

our stacked cubelet's frequency channels. We set σ_{SNR} (our signal to noise ratio) to 3 to give us 3σ upper limit estimates of the mass.

We now repeat the process, but over three equal frequency bins. The results of these are shown in Figure 17. Again we see no detection in the lowest redshift bin (41 galaxies) so from this we can only gather an upper limit of the mass. In the central bin (191 galaxies) we observe a detection in the spectrum. We see a slight detection in the center of the moment map (Figure 17b), accompanied by another bright region above it. Again this secondary region is indicative of a noise peak, i.e. a bright spot in the moment map caused by abnormally high noise in some of the channels over which we are integrating. We inspected this noise peak by taking a spectrum at its location, shown in Figure 18a. We observed quite a large baseline offset, which we correct by fitting and subtracting a 2nd order polynomial. From the corrected spectrum we measure the integrated S/N over the same channels as original detection, which came to 3.51. The fact that the noise peak has a lower S/N than that of the central detection (4.65) and the presence of the large baseline offset, convinces us that our central detection is indeed significant and real. The highest redshift stack (122 galaxies) shows a clear spectral detection, but emission in the center of the map is not localised. We also observe many other bright spots in the map. We analysed two of these bright regions again (shown in Figures 18b and 18c). Both of these show signal to noise ratios which are less than, but still comparable, to the central emission. Because of the very prominent spectral detection, and the fact that the S/N of the central emission is higher, we still continue to measure the HI mass over the indicated channels in Figure 17c.

When attempting to further increase the number of bins, the number of LCBGs per stacks drop too much to produce good stacks.

In Figure 19 we plot our results from the final three stacks, along with the mass estimated from our direct detections. To better compare low and intermediate redshift LCBGs, we show the the average M_{HI} measured by Garland et al. (2004) of 20 local LCBGs using single dish observations: $\langle M_{HI} \rangle = (4.23 \pm 0.53) \times 10^9$ $M_\odot$. We also plot the average M_{HI} of the nine $z \sim 0$ LCBGs studied by Rabidoux et al. (2018) from the same sample, but

Figure	z range	ν range (MHz)	N	$\langle M_{HI} \rangle$ ($\times 10^9 M_\odot$)	S/N
15a	0.09-0.5	940-1300	396	3.47 ± 1.02	5.93
15b	0.22-0.5	940-1160	354	3.42 ± 1.10	5.25
16a	0.22-0.35	1050-1160	127	< 3.87	2.25
16b	0.35-0.5	940-1050	227	3.36 ± 1.07	4.73
17a	0.22-0.3	1086-1160	41	< 4.89	-1.04
17b	0.3-0.4	1013-1086	191	2.49 ± 0.75	4.65
17c	0.4-0.5	940-1013	122	6.44 ± 2.71	5.62

Table 3: The properties of each of our individual stacks. The first column represents the figure that corresponds to each stack. S/N is the integrated signal to noise ratio of each peak.

using interferometry: $\langle M_{HI} \rangle = (4.21 \pm 1.07) \times 10^9$ M$_\odot$. The LCBGs from these samples were all directly detected. As we can see in the plot, we do not see signs of evolution in the HI mass of LCBGs between $0 < z < 0.5$. The average, stacked values are comparable to those directly measured at lower z. Our results are effected by the artifacts in the stacked moment 0 maps, but the detections in our stacked spectra makes us confident that our values are reasonable. A larger sample of LCBGs would help us constrain the evolution even further. More local LCBGs would give better, direct view on the masses of these systems, and more intermediate LCBGs would improve the statistics in our stacks.

‘

3.2 Star formation in LCBGs

3.2.1 LCBG star formation rates

The star formation rate (SFR) of a galaxy tells us how rapidly it is converting gas into stars. LCBGs have higher SFRs than other galaxies, making them starburst galaxies. It is this active star formation that results in the presence of many blue young stars, and hence the blue nature of LCBGs. There are many ways to estimate the star formation rate of a galaxy. Observed in the L-band, CHILES Con Pol gathered largely non-thermal, synchrotron emission (Luber et al. in prep, Gim et el. in prep). This emission in the galaxies we observe, are due to Type II supernovae. This is when massive stars violently explode after its core collapses. What is left af-

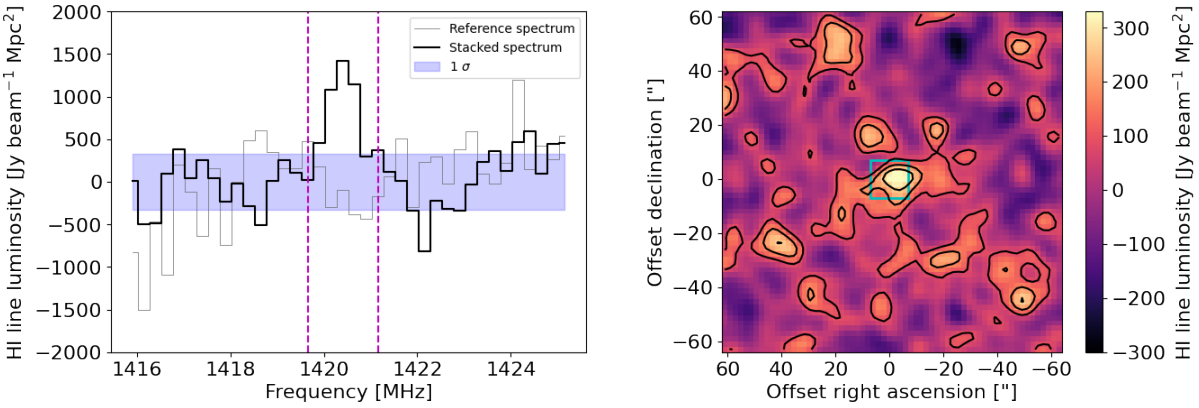

(a) The stack of 396 LCBGs between $0.09 < z < 0.5$. A clear detection is seen in the spectrum, as well as the moment 0 map.

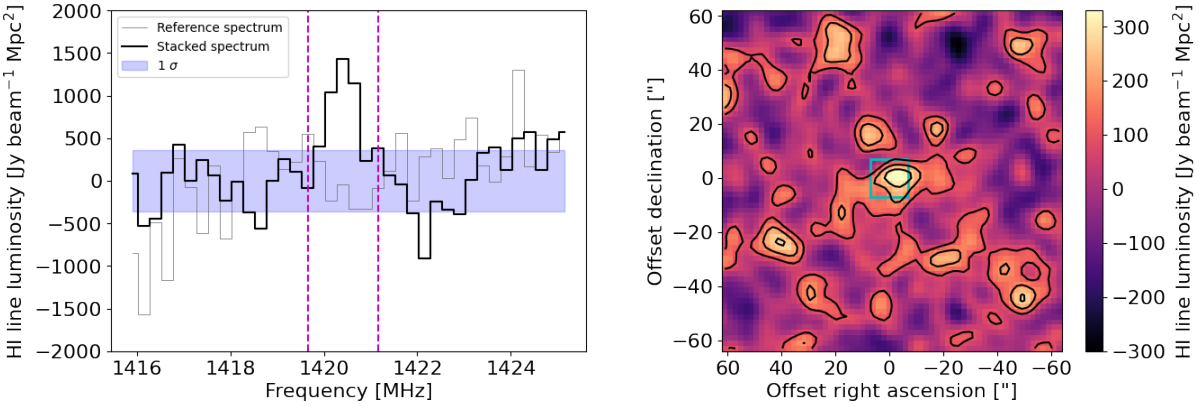

(b) The stack of 354 LCBGs between $0.22 < z < 0.5$. Again a clear detection is seen in the spectrum, as well as the moment 0 map.

Figure 15: In each panel we show the integrated, stacked spectrum from a stacked cubelet, smoothed to 50km/s. The spectrum is taken from the region indicated by the cyan box. We also show a spectrum taken away from the center of the cubelet for reference. The filled purple region indicates the off-line RMS of the spectrum. The moment 0 map on the right of each panel is produced from the channels between the dashed lines

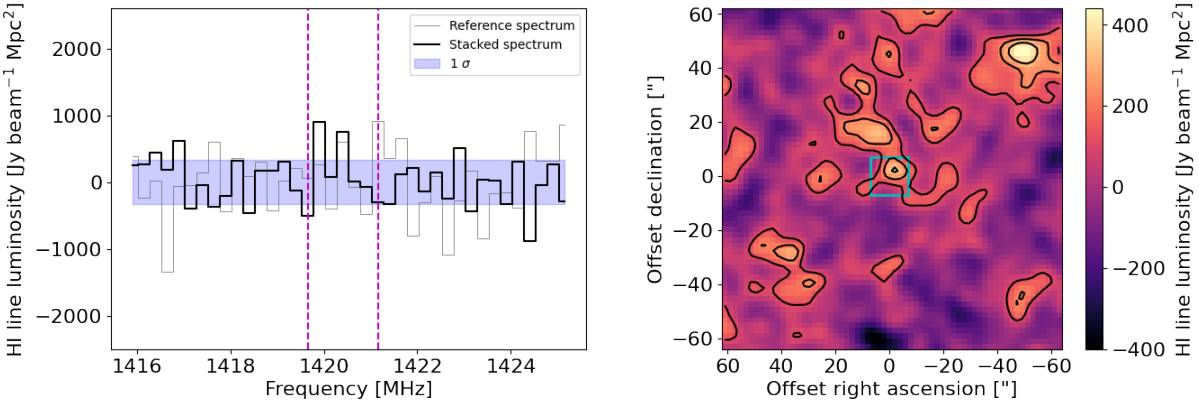

(a) The stack of 127 LCBGs bewteen $0.22 < z < 0.35$. No clear detection is observed.

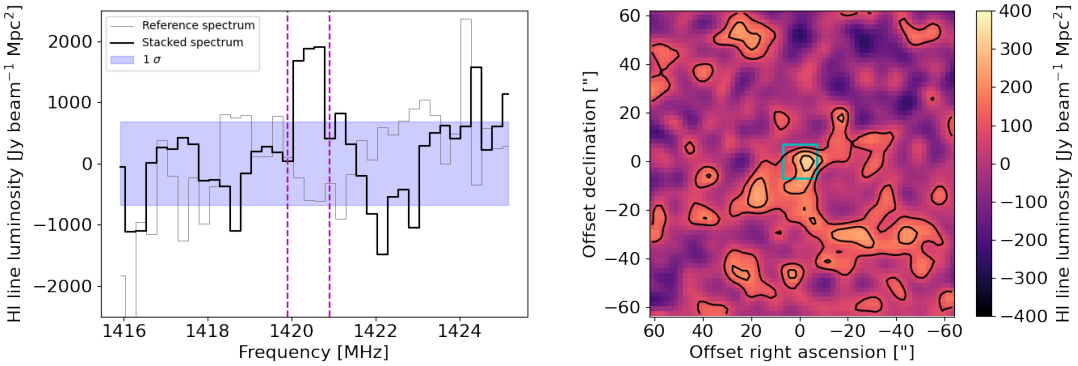

(b) The stack of 227 LCBGs bewteen $0.35 < z < 0.5$. We observe a detection in the spectrum. The moment 0 map seems to show increased intensity at the center of the cubelet, also indicative of a detection.

Figure 16: Stacks of the same sample as in Figure 15b, but now split over two, equal frequency bins: $940 < \nu < 1050$ and $1050 < \nu < 1160$.

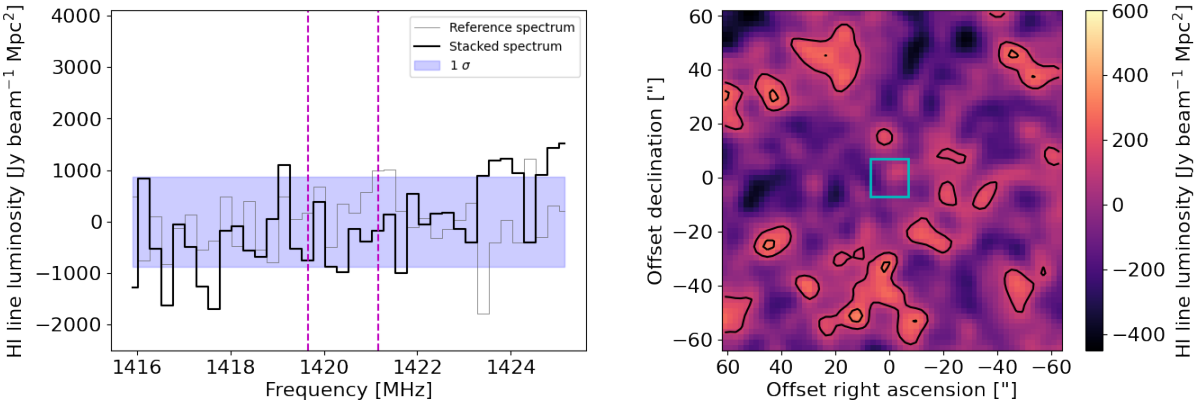

(a) The stack of 41 LCBGs between $0.22 < z < 0.3$. We see no detection in this stack.

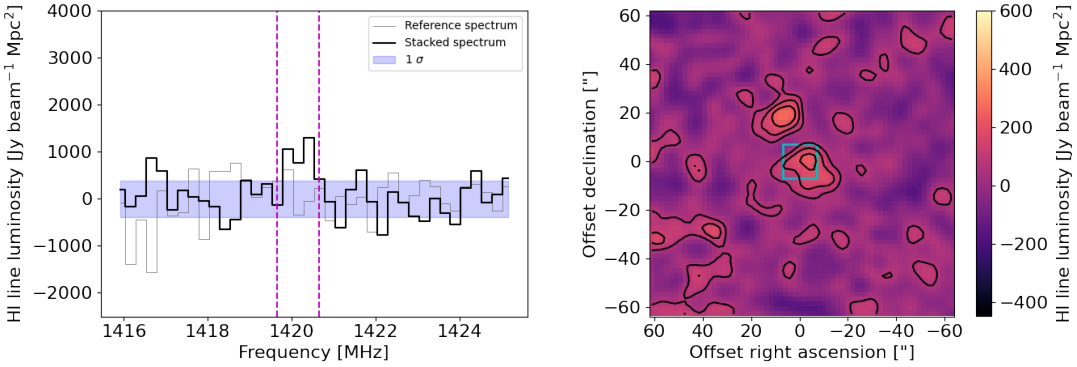

(b) The stack of 191 LCBGs between $0.3 < z < 0.4$. We observe a detection in the spectrum. We also see peaked emission in the center of the moment 0 map.

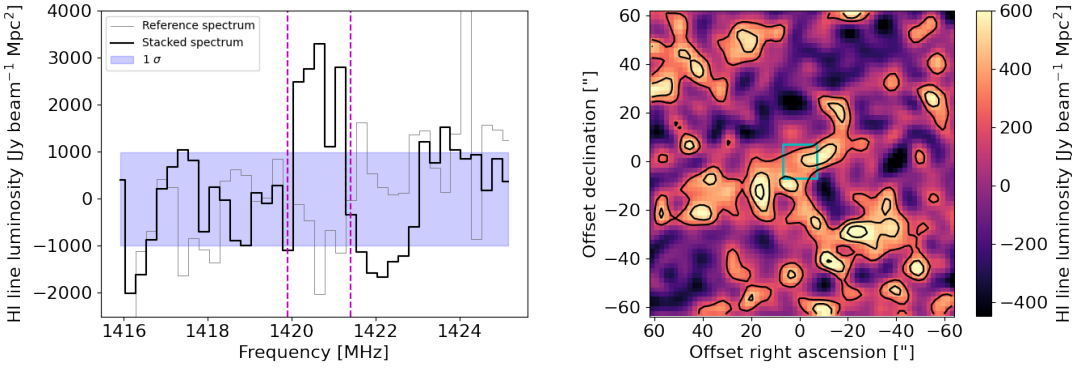

(c) The stack of 122 LCBGs bewteen $0.4 < z < 0.5$. We observe a clear detection in the spectrum.

Figure 17: Stacks of the same sample as in Figure 15b, but now split over three, equal frequency bins: $940 < \nu < 1013$, $1013 < \nu < 1086$ and $1086 < \nu < 1160$.

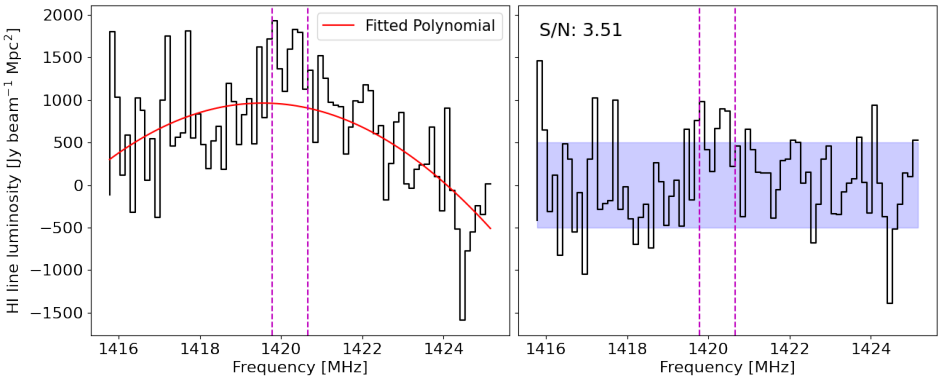

(a) Spectrum taken from the noise peak in Figure 16b located at (8",18") in the moment 0 map.

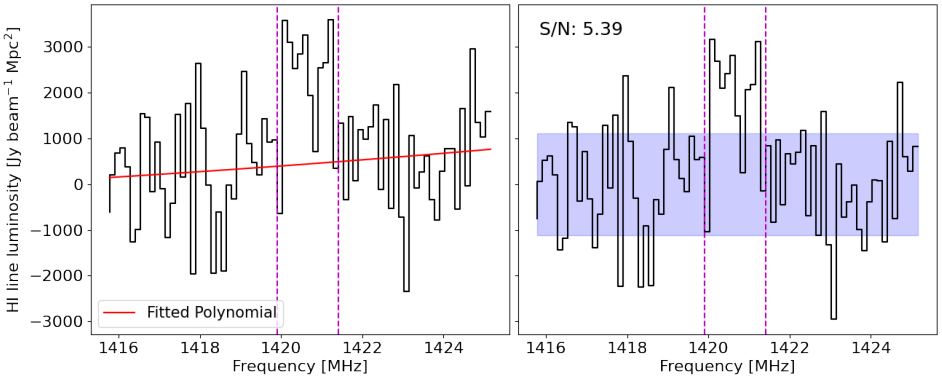

(b) Spectrum taken from the noise peak in Figure 17b located at (18",-15") in the moment 0 map.

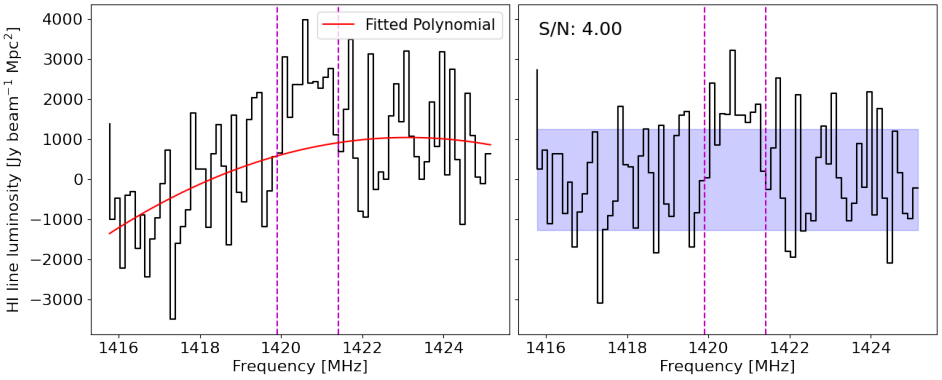

(c) Spectrum taken from the noise peak in Figure 17c located at (-22",-30") in the moment 0 map.

Figure 18: Spectra taken at noise peaks present in the moment 0 maps shown in Figures 17b and 17c. Each spectrum is baseline corrected by subtracting a fitted 2nd order polynomial. The integrated signal to noise is calculated of the region spanning the same channels as that of the central peak in each stack. This value is shown in each plot.

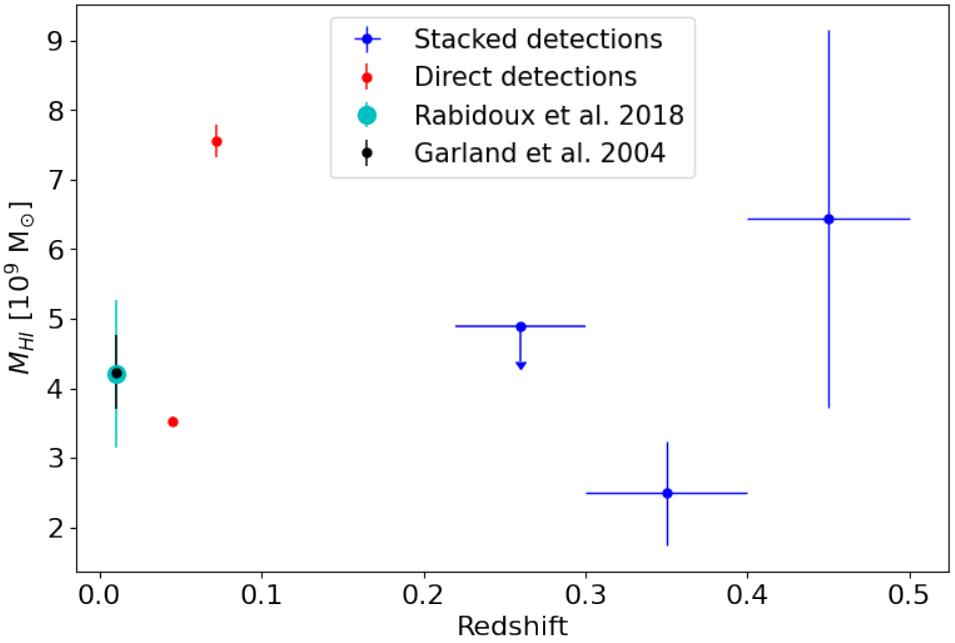

Figure 19: Our M_{HI} results from our directly detected sources, as well as from our stacked spectra in the case where we split our sample into three, equal frequency bins. For comparison we include the average HI mass of the sample of local, directly detected LCBGs studied by Garland et al. (2004) and Rabidoux et al. (2018).

ter the explosion is known as the supernova remnant (SNR). SNRs always emit synchrotron radiation as the electrons of expelled material interact with the magnetic fields in the ISM. It is the radiation that we detect from SNRs that can give us insight into the rate of stars going supernova in a galaxy. The derivation of how 1.4 GHz luminosity relates to SFR through the supernova rate is shown in detail in Hunt (2017) and Condon (1992). We measured our star formation rates in a similar fashion:

$$\frac{SFR}{M_\odot/yr} = 5.99 \times 10^{-22} \left(\frac{\nu}{GHz}\right)^{\alpha} \left(\frac{4\pi}{(1+z)^{1+\alpha}}\right) \left(\frac{D_L}{Mpc}\right)^2 \left(\frac{F_{obs}}{Jy}\right) \quad (3.6)$$

Here, ν is the rest frame frequency of the galaxy, D_L is the luminosity distance, F_{obs} is the observed 1.4 GHz flux density and α is the non-thermal spectral index. In the Milky Way and in most other sources that emit synchrotron radiation at 1 GHz, $\alpha \approx 0.8$.

We found that 1176 LCBGs lie within the CHILES region. Not all of the LCBGs that we intended to analyse were detected. The detected

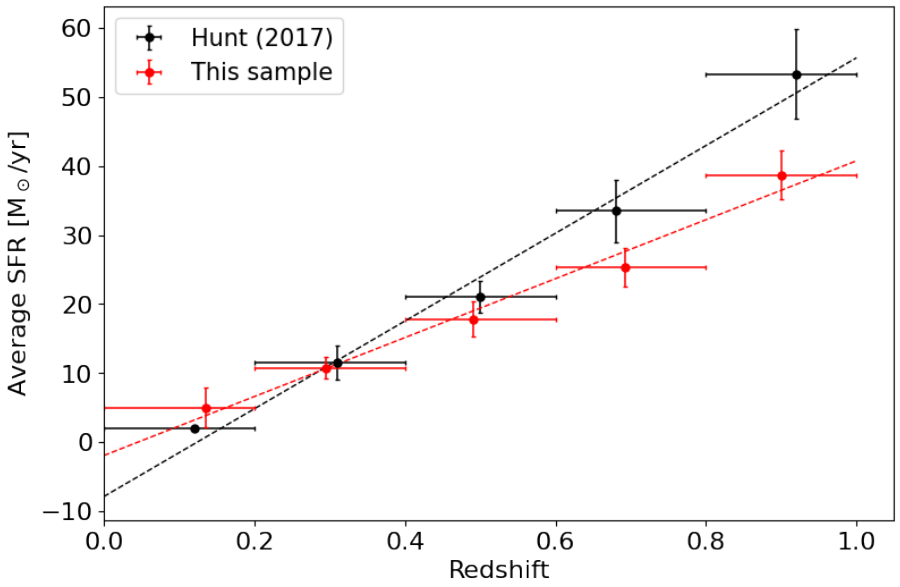

Figure 20: The average SFRs split over five redshift bins. Each data point is located at the median redshift of that bin. Also shown are the measured values from Hunt (2017).

galaxies were identified by cross-referencing our sample to a catalog of detected sources in CHILES Con Pol made by Gim et al. (in prep). Of their detections, 153 were LCBGs. The flux densities of the LCBGs within the FWHM of the CHILES Con Pol primary beam, spanning $0 < z < 1$, were measured and used to calculate their SFRs using equation 3.6. The average SFR values were calculated in five bins across our redshift range. This is shown in Figure 20. We compare our results with those obtained in Hunt (2017). In their study they measured the SFRs of 61 LCBGs in the same field. This was done using only the first epoch of CHILES data. We can see in Figure 20 that our measurements confirm that the SFR of LCBGs evolve in our redshift range. The gradient of our evolution is smaller ($m \approx 43$) than that measured by Hunt (2017) ($m \approx 64$). Here m refers to the slope in each case, measured via a least squares fitting technique.

3.2.2 Continuum Stacking

The stacking of continuum fluxes, like HI spectra or cubelets, results in an average flux which can be used to measure the average properties of a sample of sources. The objects observed in continuum can be influenced

Redshift	**N**	**Average** $M_\odot/yr$	**Median** $M_\odot/yr$	**Range** $M_\odot/yr$
$0.0 \leq z \leq 0.2$	7	5.0 ± 2.7	2.1	$0.7 \leq SFR \leq 23.5$
$0.2 < z \leq 0.4$	38	10.8 ± 1.5	8.1	$2.1 \leq SFR \leq 47.2$
$0.4 < z \leq 0.6$	24	17.8 ± 2.5	13.5	$6.1 \leq SFR \leq 51.7$
$0.6 < z \leq 0.8$	46	25.4 ± 2.8	19.9	$6.1 \leq SFR \leq 95.0$
$0.8 < z \leq 1.0$	38	38.7 ± 3.5	32.9	$16.8 \leq SFR \leq 106.9$

Table 4: Statistics of the star formation rates in our sample of 131 LCBGs.

by the telescope sensitivity, noise and confusion. Continuum stacking can help us measure properties in objects that would otherwise not have been accessible. The procedure we use is similar to that done with HI. The coordinates of galaxies in the desired field are used to extract an area around each source. The area around each source was set to be 16×16 pixels. This area is kept constant, because most of the sources are approximately equal to the size of the synthesized beam. The primary beam correction, equation 3.2, is then calculated at each of these coordinates. As before, the data is again converted into luminosity density units of Jy Mpc^2. These images are then co-added using equation 3.4 where the weights are calculated through equation 3.3. This results in a final stacked image.

To study how the stacked SFRs evolve, we binned our galaxies to ensure enough galaxies per bin, but also to have enough bins to properly trace the evolution with redshift. We choose to omit stacking between $0 < z < 0.2$ due to a lack of statistics to make up a meaningful stack. This resulted in 8 equally sized bins spanning $0.2 < z < 1.0$. Of the total of 1169 LCBGs in this range, 146 were directly detected in CHILES Con Pol. We continue to stack all of the LCBGs in our sample. Including the 'detected' and 'non-detected' galaxies. We then split this sample up in to only 'detected' and only 'non-detected'. These stacks are shown in Figure 21. We continue to measure star formation rates from these stacks using:

$$\frac{\langle SFR \rangle}{M_\odot/yr} = 5.99 \times 10^{-22} \left(\frac{\nu}{GHz}\right)^{\alpha} \left(\frac{4\pi}{(1+z)^{1+\alpha}}\right) \left(\frac{\langle S \rangle}{JyMpc^2}\right) \tag{3.7}$$

α is the same as before: 0.8 and $\langle S \rangle$ is the stacked 1.4 GHz flux. The calculated SFRs are shown in Figure 22. We see an increase in SFR towards higher redshifts in both the detected and non-detected LCBGs. The results

from the non-detected galaxies are approximately an order of magnitude smaller than those detected.

The median stellar mass of our sample is 1.81×10^{10} $M_{\odot}$. To compare how the properties of LCBGs evolve across all masses, it is beneficial to compare their specific star formation rates (sSFR), which is a galaxy's SFR normalised by its stellar mass. sSFRs tend to be lower for higher mass galaxies. This is the case across all redshifts and is commonly attributed to 'downsizing': a theory that suggests that more massive galaxies are formed at higher redshifts (Cowie et al. 1996). The study of how the sSFR changes in LCBGs has to take into account both their redshift and stellar mass. This evolution was studied and quantified by Karim et al. (2011). Their results confirm their initial assumption that the dependence of sSFR on both stellar mass and redshift can be separated. The relations between these parameters can thus be studied in separate parameter spaces. What Karim et al. (2011) proposed was that the sSFR of galaxies are given by:

$$sSFR(M_*, z) = M_*^{\beta}(1+z)^n \tag{3.8}$$

The evolution is thus governed by power-laws in both M_* and z. If they are independent of each other we can write:

$$sSFR(M_*, z) \propto sSFR(M_*|_z) sSFR(z|_{M_*}) \tag{3.9}$$

This gives:

$$sSFR(z|_{M_*}) = C(M_*)(1+z)^n \tag{3.10}$$

$$sSFR(M_*|_z) = c(z)M_*^{\beta} \tag{3.11}$$

Only our sample of detected LCBGs (shown in red in Figure 22) was split into several stellar mass and redshift bins, keeping in mind that we require enough galaxies per bin to deliver a meaningful stack. We settled on the eight original redshift bins as in Figure 22 and three stellar mass bins (see Figure 24). We are only using stacking as a way of averaging our fluxes. The non-detected sources are still confusion-limited. In the case of our HI analysis, the noise in our stacked cubelets were lower than that of our

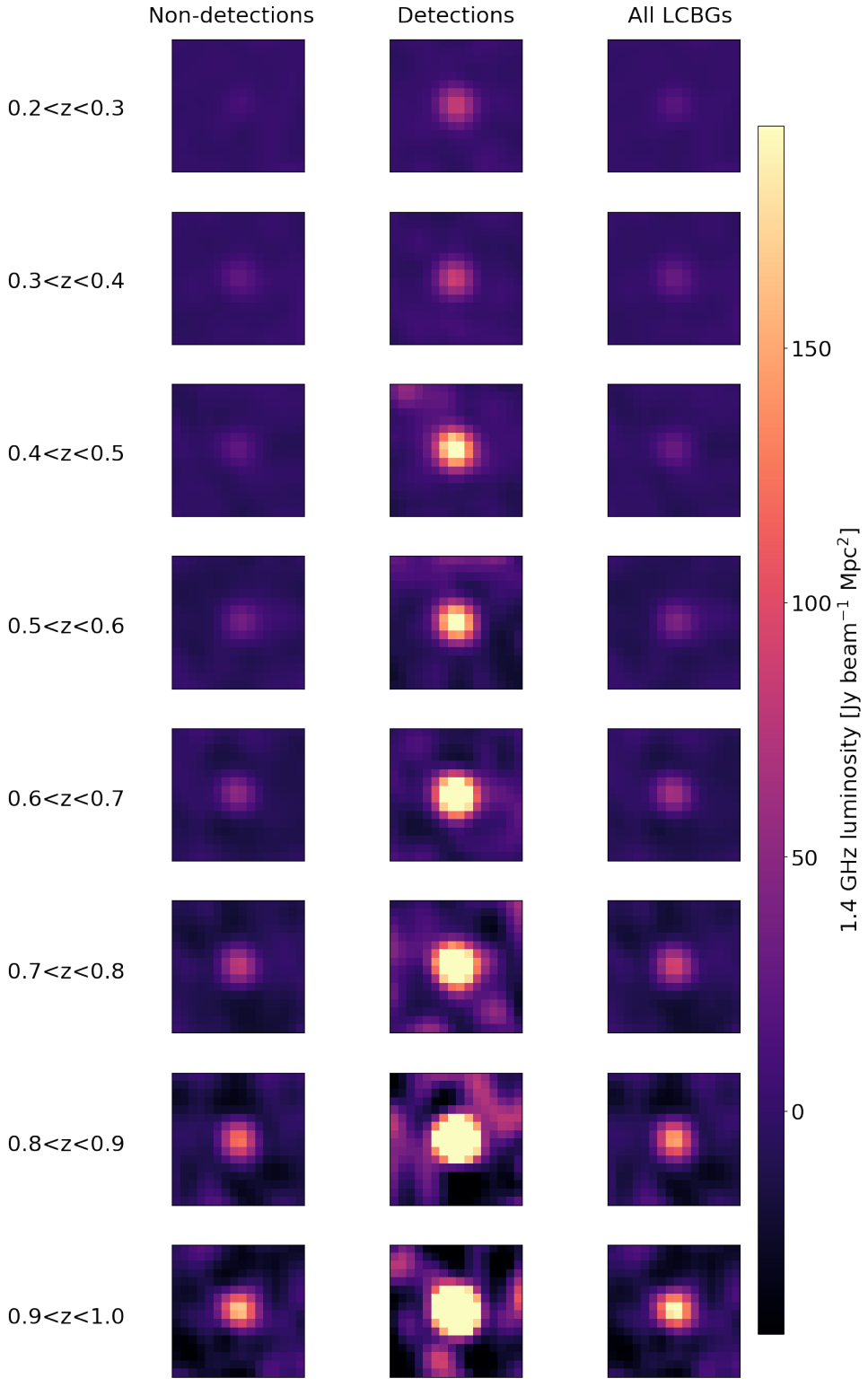

Figure 21: The stacked continuum images of our entire sample of LCBGs.

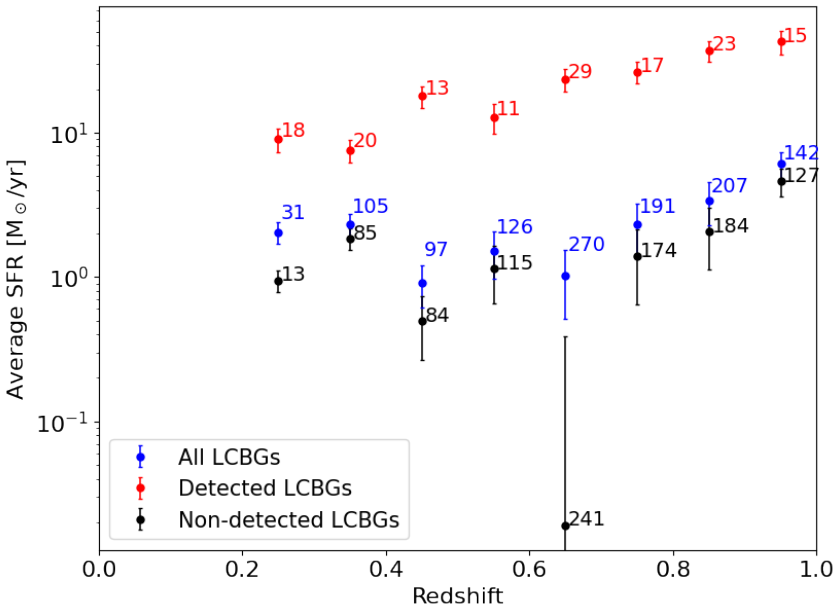

Figure 22: The average star formation rates measured from the stacked 1.4 GHz continuum fluxes. The numbers next to each data point corresponds to the number of galaxies in the stack.

original cube by a factor of $\sqrt{N}$, where N is the number of galaxies in our stack. Since our non-detected continuum sources are confusion-limited, the noise does not behave the same way. Hence, we do not include them in this analysis. We started by focusing on the sSFR's dependence of redshift. We calculated the average SFR in each redshift bin by stacking the continuum flux of each galaxy as before (Figure 23) and then divided the result by the average stellar mass of the galaxies in that sample. This gave us an evolution of average sSFR between $0.2 < z < 1$. This was repeated for three seperate stellar mass ranges: $9.6 < \log(M_*) < 10.1$, $10.1 < \log(M_*) < 10.6$ and $10.6 < \log(M_*) < 11.1$. We are excluding lowest mass LCBGs here. To quantify the evolution in each stellar mass range, we fit equation 3.10 to the calculated averages using a non-linear least squares fit. A clear evolution over cosmic time is observed and shown in Figure 25. The sSFR increases with redshift for all masses, but the rate of increase is highest for more massive galaxies. In other words, we find that the sSFR of the most massive LCBGs drops the most significantly as they evolve to the present day. The fit to these data points have two free parameters: a coefficient C and n, also referred to as the redshift-evolution parameter. Our three

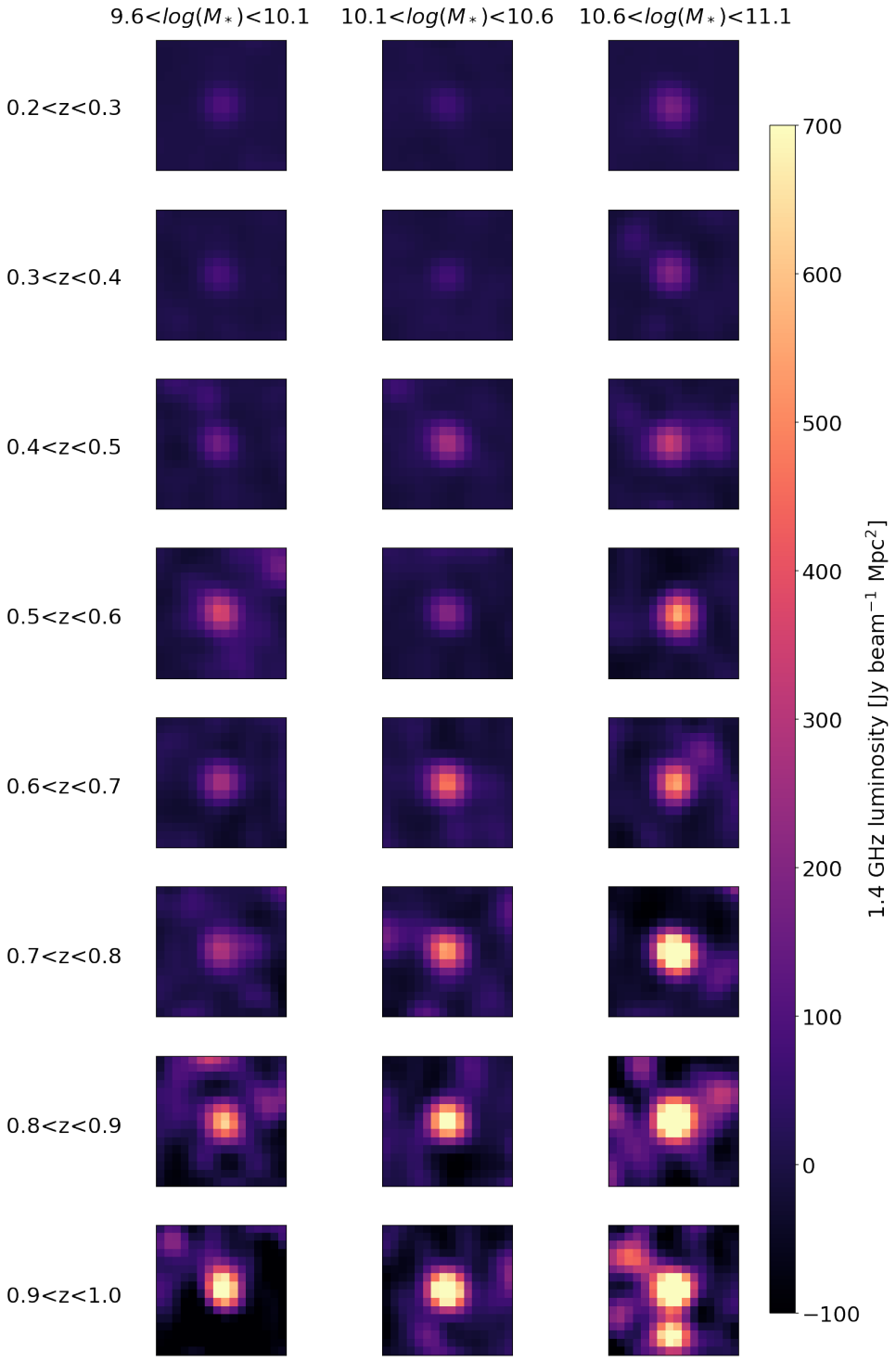

Figure 23: The stacked continuum images for our detected LCBGs across all redshift and stellar mass bins used in our analysis.

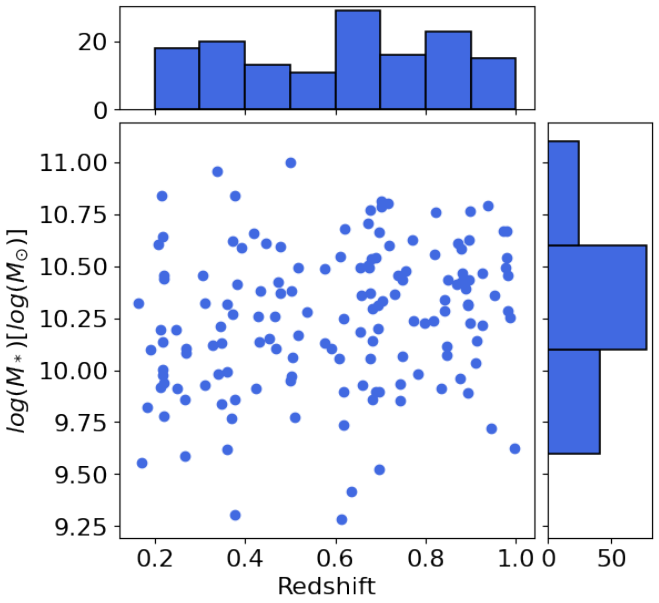

Figure 24: The distribution of LCBG stellar masses and redshifts. The sample has an average stellar mass value value of 5.12×10^9 $M_\odot$ and a median of 5.25×10^9 $M_\odot$. The histograms show the number of LCBGs in our selected binning scheme. We are excluding the lower mass LCBGs in order to have enough numbers in our stacking bins.

measured values for n are shown in Table 5.

Stellar mass range	C [1/Gyr]	n	χ^2/dof
$9.6 < \log(M_*) < 10.1$	0.29 ± 0.10	5.33 ± 0.86	2.2
$10.1 < \log(M_*) < 10.6$	0.11 ± 0.05	5.90 ± 0.86	0.8
$10.6 < \log(M_*) < 11.1$	0.06 ± 0.05	6.53 ± 1.98	23.2
Average	0.15 ± 0.06	5.92 ± 0.28	

Table 5: The fitted parameters to sSFR as a function of redshift.

Next, we calculate how the average stacked sSFR changes for galaxies between $9.6 < \log(M_*) < 11.1$. These measurements were repeated in eight redshift bins of width 0.1. Again we sought out to quantify this relationship, now by fitting 3.11 to each of these points. This fit was done exactly the same as prior, resulting in best fit parameters c and β for each redshift bin. The values are tabulated in Table 6. We were not able to do a successful fit of the data between $0.5 < z < 0.6$ due to low statistics. We find that the sSFR of LCBGs decrease with increasing stellar mass across all redshifts (see Figure 26). At lower redshifts, their sSFRs start off higher on average, decreasing more sharply towards the high-mass end.

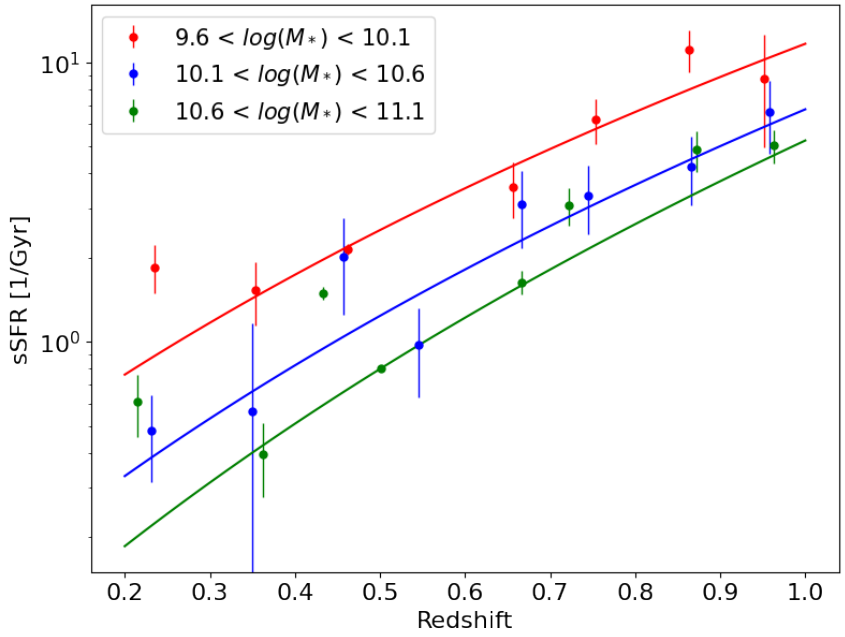

Figure 25: The evolution of sSFR as a function of redshift for three different stellar mass bins. The steady increase in sSFR with redshift is clearly seen across all masses. The fitted functions $C(M_*)(1+z)^n$ for each mass bin are shown.

Redshift range	$\log(c$ [1/Gyr])	β	χ^2/dof
$0.2 < z < 0.3$	7.57 ± 8.79	-0.75 ± 0.72	7.3
$0.3 < z < 0.4$	6.36 ± 6.97	-0.63 ± 0.17	0.8
$0.4 < z < 0.5$	2.58 ± 2.12	-0.23 ± 0.01	0.1
$0.6 < z < 0.7$	5.04 ± 5.49	-0.45 ± 0.12	0.8
$0.7 < z < 0.8$	4.60 ± 5.03	-0.38 ± 0.11	0.7
$0.8 < z < 0.9$	6.08 ± 6.93	-0.51 ± 0.29	3.4
$0.9 < z < 1.0$	4.02 ± 4.11	-0.31 ± 0.05	0.1
Average	6.76 ± 6.68	-0.46 ± 0.06	

Table 6: The fitted parameters to sSFR as a function of stellar mass.

We were interested to see how the values for n and β, which govern the sSFR evolution of LCBGs, compare to those measured in other galaxies. We make comparisons to three separate studies in Figure 27. Karim et al. (2011) was the first to do this kind of study. They also used 1.4 GHz data centered in the COSMOS field. They calculated sSFR relations for their entire sample, as well as for only star forming galaxies. We compare ours to only to the latter. Zwart et al. (2014) did a similar stacking analysis in the XMM–LSS field and also single out star forming galaxies. Ocran et al. (2023) on the other hand did their analysis using 610 MHz contin-

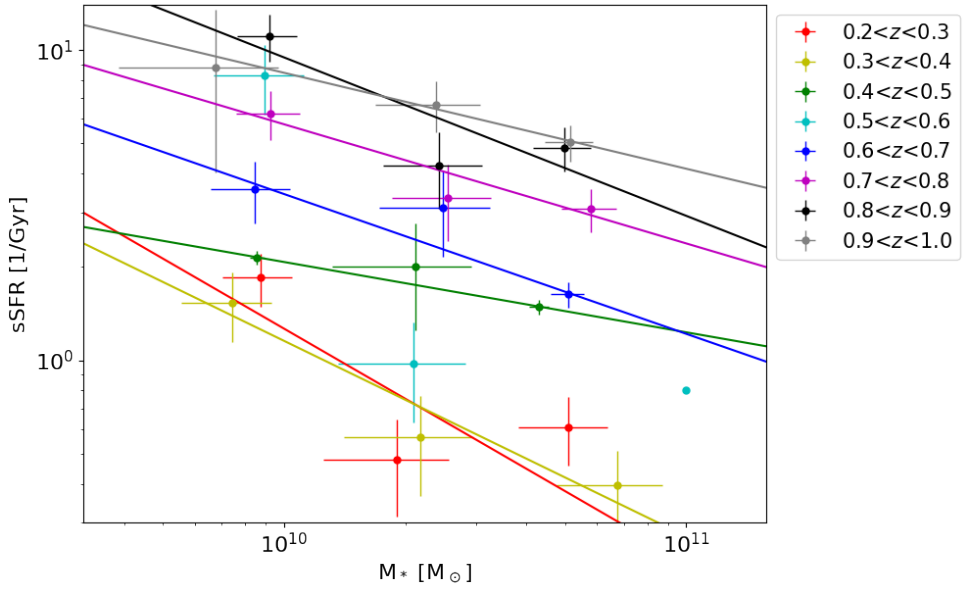

Figure 26: The evolution of sSFR as a function of stellar mass. The fitted functions $c(z)M_*^{\beta}$ for each redshift bin are shown. The data points between $0.5 < z < 0.6$ (cyan) could not be fitted to.

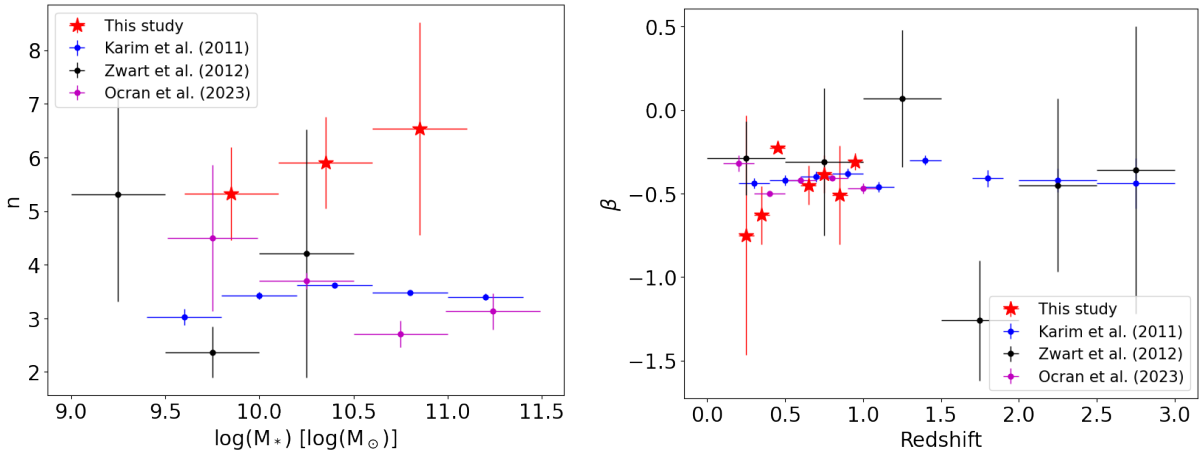

(a) (b)

Figure 27: Our measured best fit values of n and β compared three other studies. All galaxies that are being compared are actively forming stars. Our results agree, with the only discrepancy being towards the high-mass end in (a).

uum data, centred in the ELAIS-N1 region. Our measured values for the redshift-evolution parameter, n, seems to be higher on average than those measured in other studies. We also note a slight increase as the average mass increases, while those in the other samples show a slight decrease or remains constant. Our average value of n for our whole sample of LCBGs is 5.92 ± 0.28. Our values for β are fairly constant with those in the literature. We find that this value remains fairly constant up to $z = 1$ with some scatter. All our values are negative and the average for our whole sample is -0.46 ± 0.06. These results are in favour of the 'downsizing' theory explained prior.

Chapter 4

Conclusion

In this study, we set out to trace the evolutionary properties of Luminous Compact Blue Galaxies at radio frequencies within the COSMOS field. The deep-field CHILES survey gave us the opportunity to study the neutral hydrogen properties of LCBGs up to redshifts of 0.5. By means of the hydrogen 21 cm emission line, we were able to directly detected hydrogen in three LCBGs at $z = 0.045$, $z = 0.072$ and $z = 0.219$. All three showed clear rotation and undisturbed velocity gradients throughout the galaxies. The gas of the two lower redshift sources coincided nicely with each galaxy's stellar component. The neutral hydrogen in the higher redshift source seemed to be uniformly offset from its stellar component and we suspect we are observing an interaction of the LCBG with a non-LCBG neighbour. We measured each of their HI masses. These masses agree with what has been previously measured in local LCBGs. To obtain higher redshift HI measurements, we implemented a cubelet stacking technique and stacked LCBGs in bins of equal frequency between $0.22 < z < 0.5$. Some of these stacks were successful and showed a clear peak in the stacked spectrum at 1420 MHz. From these stacks we determined the average HI mass of the galaxies that make up the stack. From the unsuccessful stacks, we continued to measure upper limits for their masses. When comparing the stacked masses with the locally detected masses, we observe no clear evolution across cosmic time. We also explored the radio continuum emission from LCBGs, meausred in the CHILES Continuum Polarisation survey. From the 1.4 GHz fluxes, we measured star formation rates in individual

LCBGs between $0 < z < 1$. Our results agreed with similar measurements done from the first epoch of the survey. We observed an increase in star formation rate with redshift. We then implemented stacking on various samples of LCBG continuum fluxes, binned according to both redshift, as well as stellar mass. From each of these stacks we measured the average specific SFR. We observed clear evolution of sSFR with respect to redshift in three different stellar mass samples. The sSFR of LCBGs increase with redshift, and this increase is steeper for higher mass galaxies. We measure a decrease in the sSFR with higher mass galaxies which are at approximately the same redshift. As a means of quantifying the evolution of sSFR in these two parameter spaces, we calculate the average redshift evolution parameter for LCBGs to be $\langle n \rangle = 5.92 \pm 0.28$ and the average stellar mass evolution index to be $\langle \beta \rangle = -0.46 \pm 0.06$. Our results are in favour of the theory of cosmic downsizing: the most massive LCBGs form their stars at higher redshifts and more efficiently than low mass galaxies.

4.1 Future work

Our study of LCBGs was mainly limited by the number of them available within the CHILES region in COSMOS. The very nature of LCBGs make them rarer in the local universe. In the future, we would like the make use of larger surveys to boost the statistics of studing LCBGs. Two radio surveys currently underway are ideal for this study: MIGHTEE-HI, which is a wide field survey of several regions in the sky, including COSMOS, as well as LADUMA, which is an ultra deep-field survey aiming at probing HI out to $z > 1$. Both of these surveys are being undertaken by the MeerKAT telescope in South Africa. The wide field of view of MIGHTEE-HI would allow more more local LCBGs to be directly detected, solving our problem of low number densities at low redshifts. LADUMA would allow us to probe even deeper into the distant universe, giving us the opportunity to study the evolution of the earliest LCBGs when they were the most abundant.

Bibliography

Bera et al. (2022), 'The HI mass function of star-forming galaxies at $z \sim 0.35$', *The Astrophysical Journal Letters* **940**(1), L10.

Blue Bird et al. (2020), 'Chiles VI: HI and Hα observations for $z < 0.1$ galaxies; probing hi spin alignment with filaments in the cosmic web', *Monthly Notices of the Royal Astronomical Society* **492**(1), 153–176.

Cardamone et al. (2009), 'Galaxy zoo green peas: discovery of a class of compact extremely star-forming galaxies', *Monthly Notices of the Royal Astronomical Society* **399**(3), 1191–1205.

Carroll, B. & Ostlie, D. (2017), *An introduction to modern astrophysics*, Cambridge University Press.

Chandra et al. (2004), 'The late-time radio emission from SN 1993J at meter wavelengths', *The Astrophysical Journal* **612**(2), 974.

Chen et al. (2021*a*), 'Interferometric cubelet stacking to recover HI emission from distant galaxies', *Monthly Notices of the Royal Astronomical Society* **502**(2), 2308–2318.

Chen et al. (2021*b*), 'Measuring cosmic density of neutral hydrogen via stacking the DINGO-VLA data', *Monthly Notices of the Royal Astronomical Society* **508**(2), 2758–2770.

Chengalur et al. (2001), 'HI in Abell 3128', *arXiv preprint astro-ph/0104331* .

Cimatti, Fraternali & Nipoti (2019), *Introduction to galaxy formation and evolution: From primordial gas to present-day galaxies*, Cambridge University Press.

Coil et al. (2011), 'The PRISM Multi-Object Survey (PRIMUS). I. Survey Overview and Characteristics', *The Astrophysical Journal* **741**(1), 8.

Comrie et al. (2021), 'IDAVIE-v: Immersive Data Visualisation Interactive Explorer for Volumetric Rendering', *Zenodo* .

Condon, J. (1992), 'Radio emission from normal galaxies', *Annual review of astronomy and astrophysics* **30**(1), 575–611.

Condon, J. & Ransom, S. (2016), *Essential radio astronomy*, Vol. 2, Princeton University Press.

Cowie et al. (1996), 'New insight on galaxy formation and evolution from keck spectroscopy of the hawaii deep fields', *arXiv preprint astro-ph/9606079* .

Crawford et al. (2011), 'Spectroscopy of luminous compact blue galaxies in distant clusters. I. spectroscopic data', *The Astrophysical Journal* **741**(2), 98.

Crawford. et al. (2014), 'Spatial and kinematic distributions of transition populations in intermediate redshift galaxy clusters', *The Astrophysical Journal* **786**(1), 30.

Crawford et al. (2016), 'Spectroscopy of luminous compact blue galaxies in distant clusters. II. physical properties of dE progenitor candidates', *The Astrophysical Journal* **817**(2), 87.

Davé et al. (2017), 'MUFASA: galaxy star formation, gas and metal properties across cosmic time', *Monthly Notices of the Royal Astronomical Society* **467**(1), 115–132.

Davies et al. (2015), 'Galaxy and mass assembly (GAMA): the effect of close interactions on star formation in galaxies', *Monthly Notices of the Royal Astronomical Society* **452**(1), 616–636.

De Hoyos (2006), On the Nature of Distant Luminous Compact Blue Galaxies, PhD thesis, Department of Physical Sciences, Autonomous University of Madrid.

Delhaize et al. (2013), 'Detection of HI in distant galaxies using spectral stacking', *Monthly Notices of the Royal Astronomical Society* **433**(2), 1398–1410.

Driver et al. (2011), 'Galaxy and mass assembly (GAMA): survey diagnostics and core data release', *Monthly Notices of the Royal Astronomical Society* **413**(2), 971–995.

Fernández et al. (2013), 'A pilot for a Very Large Array HI deep field', *The Astrophysical Journal Letters* **770**(2), L29.

Fernández et al. (2016), 'Highest redshift image of neutral hydrogen in emission: a CHILES detection of a starbursting galaxy at $z = 0.376$', *The Astrophysical Journal Letters* **824**(1), L1.

Gallego (2009), Three-dimensional kinematics of local luminous compact blue galaxies, PhD thesis, University of Florida.

Garland et al. (2004), 'The nature of nearby counterparts to intermediate-redshift luminous compact blue galaxies. I. Optical/HI properties and dynamical masses', *The Astrophysical Journal* **615**(2), 689.

Garland et al. (2005), 'The nature of nearby counterparts to intermediate-redshift luminous compact blue galaxies. II. CO observations', *The Astrophysical Journal* **624**(2), 714.

Garland et al. (2015), 'Nearby clumpy, gas rich, star-forming galaxies: Local analogs of high-redshift clumpy galaxies', *The Astrophysical Journal* **807**(2), 134.

Gould (1994), 'Radiative hyperfine transitions', *The Astrophysical Journal* **423**, 522–528.

Guzmán et al. (1997), 'The nature of compact galaxies in the hubble deep field. II. Spectroscopic properties and implications for the evolution of the star formation rate density of the universe', *The Astrophysical Journal* **489**(2), 559.

Guzmán et al. (2003), 'Stellar masses of luminous compact blue galaxies at redshifts $z = 0.4 - 1.2$', *The Astrophysical Journal* **586**(1), L45.

Hammer et al. (2001), 'Luminous compact galaxies at intermediate redshifts: progenitors of bulges of massive spirals?', *The Astrophysical Journal* **550**(2), 570.

Heckman et al. (2005), 'The properties of ultraviolet-luminous galaxies at the current epoch', *The Astrophysical Journal* **619**(1), L35.

Hess et al. (2019), 'CHILES: HI morphology and galaxy environment at $z = 0.12$ and $z = 0.17$', *Monthly Notices of the Royal Astronomical Society* **484**(2), 2234–2256.

Hunt (2017), The Evolution of Luminous Compact Blue Galaxies in COSMOS between $z = 0.0 - 1.0$, PhD thesis, West Virginia University.

Hunt et al. (2021), 'The evolution of the luminosity function for luminous compact blue galaxies to $z = 1$', *The Astrophysical Journal* **909**(1), 49.

Jones et al. (2018), 'The ALFALFA HI mass function: a dichotomy in the low-mass slope and a locally suppressed 'knee' mass', *Monthly Notices of the Royal Astronomical Society* **477**(1), 2–17.

Karim et al. (2011), 'The star formation history of mass-selected galaxies in the COSMOS field', *The Astrophysical Journal* **730**(2), 61.

Koekemoer et al. (2007), 'The COSMOS survey: Hubble space telescope advanced camera for surveys observations and data processing', *The Astrophysical Journal Supplement Series* **172**(1), 196.

Koo et al. (1994), 'HST images of very compact blue galaxies at $z \approx 0.2$', *The Astrophysical Journal* **427**, L9–L12.

Lah et al. (2007), 'The HI content of star-forming galaxies at $z = 0.24$', *Monthly Notices of the Royal Astronomical Society* **376**(3), 1357–1366.

Laigle et al. (2016), 'The COSMOS2015 catalog: Exploring the $1 < z < 6$ universe with half a million galaxies', *The Astrophysical Journal Supplement Series* **224**(2), 24.

Lilly et al. (2007), 'zCOSMOS: a large VLT/VIMOS redshift survey covering $0 < z < 3$ in the COSMOS field', *The Astrophysical Journal Supplement Series* **172**(1), 70.

Luber (2022), Deep Radio Observations and the Role of the Cosmic Web in Galaxy Evolution, PhD thesis, West Virginia University.

Madau & Dickinson (2014), 'Cosmic star-formation history', *Annual Review of Astronomy and Astrophysics* **52**, 415–486.

Mo, H., Van den Bosch, F. & White, S. (2010), *Galaxy formation and evolution*, Cambridge University Press.

Noeske et al. (2006), 'Luminous compact blue galaxies up to $z \approx 1$ in the hubble space telescope ultra deep field. I. Small galaxies or blue centers of massive disks?', *The Astrophysical Journal* **640**(2), L143.

Ocran et al. (2023), 'Star Formation History of $0.1 \leq z \leq 1.5$ Mass-Selected Galaxies in the ELAIS-N1 Field', *Monthly Notices of the Royal Astronomical Society* **524**(4), 5229–5247.

Phillips et al. (1997), 'The nature of compact galaxies in the hubble deep field. I. Global properties', *The Astrophysical Journal* **489**(2), 543.

Rabidoux et al. (2018), 'Resolved HI observations of local analogs to $z \approx 1$ luminous compact blue galaxies: Evidence for rotation-supported disks', *The Astrophysical Journal* **852**(2), 125.

Randriamampandry et al. (2017), 'Star-forming galaxies in intermediate-redshift clusters: stellar versus dynamical masses of luminous compact blue galaxies', *Monthly Notices of the Royal Astronomical Society* **470**(4), 4382–4396.

Roberts & Haynes (1994), Global properties along the morphological sequence from Im to Sa, *in* 'Dwarf Galaxies, ESO Conference and Workshop Proceedings', Vol. 49, p. 197.

Rodighiero et al. (2011), 'The lesser role of starbursts in star formation at z=2', *The Astrophysical journal letters* **739**(2), L40.

Ryden (2017), *Introduction to cosmology*, Cambridge University Press.

Schneider (2006), *Extragalactic astronomy and cosmology: An introduction*, Vol. 146, Springer.

Serra et al. (2015), 'SOFIA: a flexible source finder for 3D spectral line data', *Monthly Notices of the Royal Astronomical Society* **448**(2), 1922–1929.

Tollerud et al. (2009), 'The WHIQII survey: metallicities and spectroscopic properties of luminous compact blue galaxies', *The Astrophysical Journal* **708**(2), 1076.

Van Zee et al. (1998), 'Neutral gas distributions and kinematics of five blue compact dwarf galaxies', *The Astronomical Journal* **116**(3), 1186.

VLA Observational Status Summary (2024).
URL: *https://science.nrao.edu/facilities/vla/docs/manuals/oss*

Werk et al. (2004), 'Luminous compact blue galaxies in the local universe', *The Astrophysical Journal* **617**(2), 1.

Westmeier et al. (2021), 'SoFiA 2 - an automated, parallel HI source finding pipeline for the WALLABY survey', *Monthly Notices of the Royal Astronomical Society* **506**(3), 3962–3976.

Zwaan (2000), Atomic hydrogen in the local universe, PhD thesis, University of Groningen.

Zwart et al. (2014), 'The star formation history of mass-selected galaxies from the VIDEO survey', *Monthly Notices of the Royal Astronomical Society* **439**(2), 1459–1471.